ERDC/CRREL TR-05-3

Cold Regions Research and Engineering Laboratory

US Army Corps of Engineers®
Engineer Research and Development Center

Constitutive Model for a Thawing, Frost-Susceptible Sand

Sally Shoop, Rosa Affleck, Vincent Janoo,
Robert Haehnel, and Benjamin Barrett

February 2005

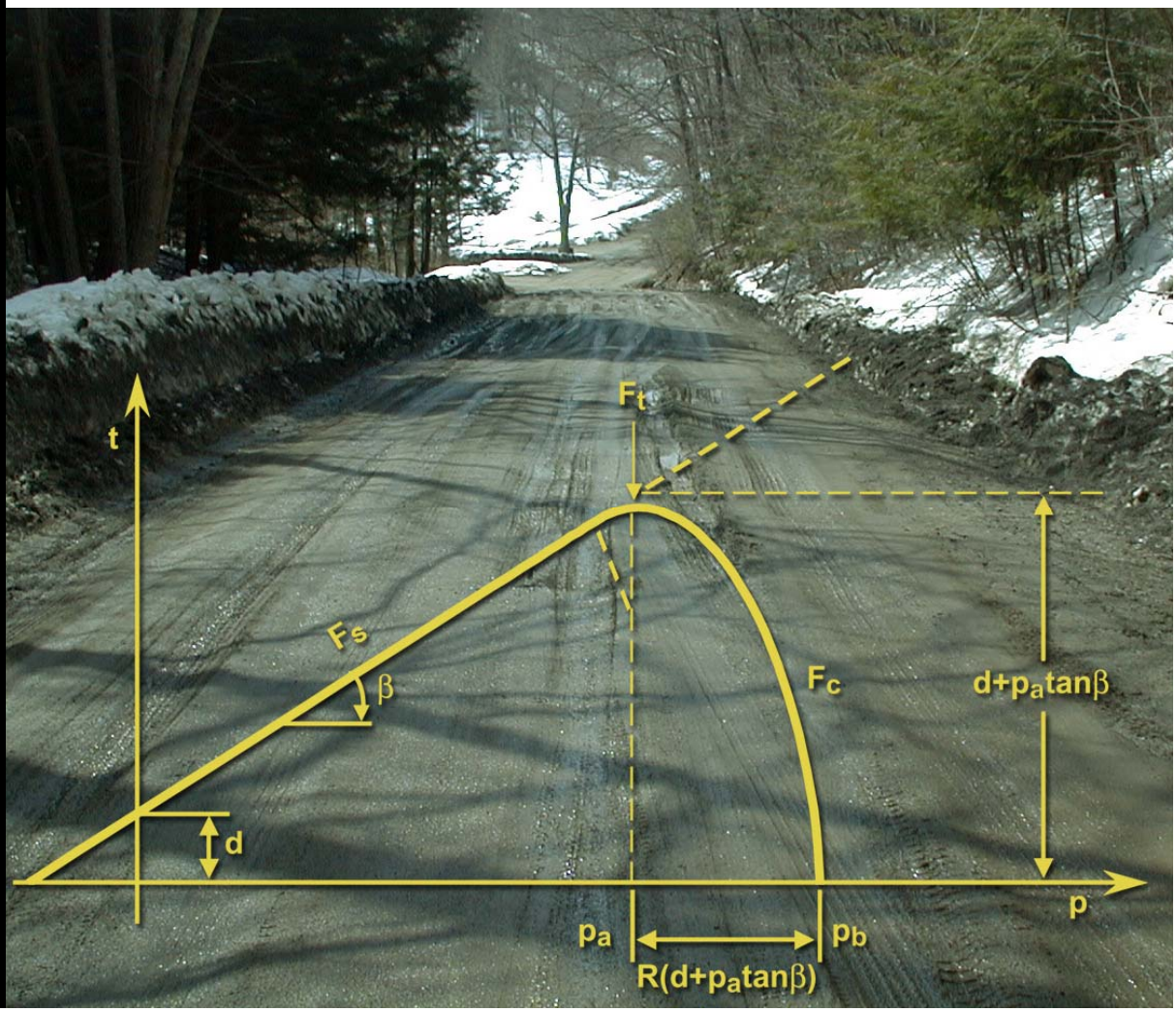

ERDC/CRREL TR-05-3
February 2005

Constitutive Model for a Thawing, Frost-Susceptible Sand

Sally Shoop, Rosa Affleck, Vincent Janoo,
Robert Haehnel, and Benjamin Barrett

Cold Regions Research and Engineering Laboratory
U.S. Army Engineer Research and Development Center
72 Lyme Road
Hanover, New Hampshire 03755

Prepared for U.S. Army Corps of Engineers
Washington, DC 20314-1000

ABSTRACT

A material model for soft, wet soil was generated to simulate the deformation behavior of thawing soil under vehicle loading on paved and unpaved roads. Freeze–thaw action produces a loose, wet soil that undergoes large deformation when subjected to vehicle loads. The soil modeled is a frost-susceptible fine sand, which was used in full-scale tests of paved and unpaved road sections in CRREL's Frost Effects Research Facility (FERF). The soil was subjected to a full suite of saturated and unsaturated triaxial testing, using density, moisture, and loading conditions duplicating those experienced during the freeze–thaw testing in the FERF. Material parameters were generated for a capped Drucker–Prager plasticity model. These were calibrated in triaxial test simulations using the commercial finite element code ABAQUS. The material model was then implemented in several three-dimensional finite element simulations for validation and robustness. The model for Lebanon Sand was compared to the same model for other granular materials.

CONTENTS

ILLUSTRATIONS

TABLES

LIST OF SYMBOLS

c	cohesion
c'	apparent cohesion
d	Drucker–Prager material cohesion
e	void ratio
E	Young's modulus
F_c	cap failure surface for compactive–dilatant failure
F_s	shear failure surface
F_t	transitional failure surface
G_s	flow potential shear surface
G_c	flow potential cap surface
I_1	trace (σ)
$\bar{I}$	identity matrix
K	flow stress ratio (related to shape of yield surface in deviatoric plane)
p	mean (total) normal stress
p'	mean effective normal stress
p_a	defines the evolution of the hardening/softening of the cap (location of Drucker–Prager cap along the mean pressure axis)
p_b	hydrostatic compression yield stress (Drucker–Prager model)
p_c	hydrostatic compression strength (foam model)
$p_c\|_0$	initial value of hydrostatic compressive stress (foam model)
p_{max}	maximum contact pressure
p_t	hydrostatic tensile yield stress
p_t^{el}	elastic tensile limit
q	deviatoric stress
R	cap eccentricity parameter (controlling the shape of the cap)
s_i	component of stress deviation ($\sigma_i - p$)
S	$\bar{S} = \bar{\sigma} + p\bar{I}$
u	pore water pressure

v	specific volume
α	parameter to smooth the transition between the shear and cap failure
β	Drucker–Prager material angle of friction
ε_{vol}^{in}	volumetric inelastic (plastic or creep) strain
$\varepsilon_{vol}^{in}\big\vert_0$	initial value of volumetric inelastic strain
ε_{vol}^{pl}	volumetric plastic strain
$\varepsilon_{vol}^{pl}\big\vert_0$	initial value of volumetric plastic strain
κ	elastic slope on the pressure–volume curve
λ	plastic slope on the pressure–volume curve
μ	coefficient of friction
ρ	density
ρ_0	initial density
σ_0	initial yield stress in uniaxial compression
σ_h	horizontal stress
σ	normal stress
σ_i	normal stress in the i direction; $i = x,y,z$ (principal stress when $i = 1,2,3$)
σ_{oct}	octahedral normal stress
σ_v	vertical stress
τ	shear stress
τ_{ij}	shear stress, $i,j = x,y,z$
τ_{oct}	octahedral shear stress
ν	Poisson's ratio
φ	friction angle
φ'	apparent friction angle

PREFACE

This report was prepared by Dr. Sally Shoop, Research Civil Engineer, Applied and Military Engineering Branch; Rosa Affleck, Research Civil Engineer, Civil and Infrastructure Engineering Branch; Dr. Vincent Janoo, formerly Research Civil Engineer, Civil and Infrastructure Engineering Branch; Robert Haehnel, Research Mechanical Engineer, Ice Engineering Group; and Benjamin Barrett, summer intern, Applied and Military Engineering Branch, all of the U.S. Army Cold Regions Research and Engineering Laboratory (CRREL), Engineer Research and Development Center (ERDC).

Funding for this work was provided by the Office of the Chief of Engineers under AT42, Joint Rapid Airfield Construction, Mechanical Behavior of Freezing/Thawing Pavement Structures.

Saturated triaxial testing for this work was proficiently performed by Richard Peterson of the Structural and Geotechnical Laboratory (at Waterways Experiment Station), Vicksburg, Mississippi. The unsaturated triaxial testing was skillfully developed and executed by Charles Smith of CRREL. The authors thank Dr. Stephen Ketcham and Dr. Raymond Rollings, both of CRREL, for their prompt and thoughtful reviews of this paper.

This report was prepared under the general supervision of Dr. Justin Berman, Chief, Applied and Military Engineering Branch; Dr. Lance Hansen, Deputy Director; and James L. Wuebben, Acting Director, CRREL.

The commander and executive director of the Engineering Research and Development Center is COL James R. Rowan, EN. The director is Dr. James R. Houston.

Constitutive Model for a Thawing, Frost-Susceptible Sand

SALLY SHOOP, ROSA AFFLECK, VINCENT JANOO,
ROBERT HAEHNEL, AND BENJAMIN BARRETT

1 INTRODUCTION

The Problem of Spring Thaw

Spring thaw is a critical time of year for the deterioration of roads and airfields. The prediction of performance, or deterioration, of pavement structures is important not only for maintenance scheduling, but also, for the military, for deployment and operations at all times of year. In developing nations the use of secondary roads and airfields for rapid deployment will be critical, and the performance of these structures must be optimized.

The types of deterioration or distresses most common during spring on secondary, unpaved roads are rutting and roughness (Shoop et al. 2002), as illustrated in Figure 1. Deformation of the road surface (either paved or unpaved) during spring thaw is nearly always the result of the deformation of the thawing layer, which has undergone a reduction in density and is often very wet or saturated as a result of the freezing process. The deformation of the loose, weak, thawing layer is largely plastic, consisting of both compaction and shear. Because the thickness of the thawing layer varies throughout the thawing season (during spring or intermittent thaws), a method to simulate the impact of both the plastic deformation and the varying layer geometry was desired. Therefore, we developed a finite element model of the layered thawing road system. The primary challenge was to capture the deformation behavior of the thawing layer, which had not been previously documented.

Figure 1. Rutting on unpaved secondary roads during spring thaw. (Photo by George Blaisdell, Hanover, NH.)

Approach to Predicting the Effects of Freeze–Thaw on Vehicle and Pavement Performance

Because of the difficult and time-consuming nature of constructing full-scale test sections and field experiments on thawing ground, we aimed to create a finite element modeling capability, validated with experimental data, that would then be useful for performing computer experiments on a wide range of off-road, pavement, and vehicle or aircraft loading situations. To do this, we first had to develop a material model to represent thawing soil, as none was available.

This paper documents the experimental development of a constitutive model representative of a typical frost-susceptible, thaw-weakening material. The soil is well characterized, with additional data provided in the appendices. Although other material models were tried, the material model chosen was a modified Capped Drucker–Prager constitutive model as implemented in the commercial finite element code ABAQUS. An extensive laboratory program to fully characterize the mechanical behavior of the soil was completed. The test methodology and results are presented, along with the material model and the calibration of the model parameters. Finally, the thawing soil material model is successfully implemented in a 3D finite element simulation of a wheel rolling on an off-road soil and a layered pavement using a model incorporating freeze–thaw layering.

2 METHODS

Material Model for Thawing Soil

The deformation of the layered pavement system during spring thaw is largely (perhaps entirely) the result of deformation of the weak, thawing layer. The thawing soil may lose compaction as a result of excess water being drawn to the freezing front, expansion during freezing, and ice lens formation. Also, the loose material is often wet or saturated during thaw when water is trapped in the thawing layer by the impermeable frozen layer below. This material deforms plastically in both compaction and shear (Shoop et al. 2003).

The major deformation modes of the thawing layer must be adequately represented by the material constitutive model. A Capped Drucker–Prager (CDP) plasticity model was chosen to capture the elastic and plastic behavior of the material under vehicle loading during spring thawing conditions (i.e. the soil may be loose, the water content is wet of optimum to fully saturated, and the loading is short term). The features of the CDP model include elastic response, hardening/softening as a function of volumetric plastic strain, inelastic behavior, and yield behavior. In the CDP model as implemented in the commercial finite element software ABAQUS (HKS 2002), the shear line is fixed (d and β are constant) and hardening (compression of the material) occurs on the cap. The parameters include

d = material cohesion

β = material angle of friction

R = cap eccentricity

λ and κ = slopes of the loading (compression) and unloading (elastic) lines

E = Young's modulus

ν = Poisson's ratio.

A good overview of the development of plasticity theory and constitutive modeling of soil is given in Scott (1985). Schofield extended plasticity theory to the critical state concept, defining either contractile or dilatant deformation of porous material as a function of its specific volume or void ratio (Schofield and Wroth 1968). In critical state theory, this rule is developed around the concept of a "critical state," where the plastic shearing deformation occurs at a constant volume. Perhaps the most famous critical state model, the Cam–clay model, was developed based on the behavior of clays. The concepts are equally applicable to defining the shearing and volumetric behavior of granular materials such as

granular soils or snow (Wood 1990). Although the concepts are applicable for both cohesive and granular materials, the behavior of the granular materials has not been explored as thoroughly, particularly regarding the influence of deviatoric stress on the yield surface, which is less clearly defined in soils but may take on a much different shape than the yield surface of metals. Wood (1990) considers this a difference in detail rather than a difference in concept.

The modified CDP model also has the features of a critical state model (i.e. regions of constant volume shear deformation and compactive–dilatant flow). The flow is non-associative (i.e. the flow potential is not associated with the yield surface), except on the cap surface of the CDP model.

The features of the model are best illustrated in terms of stress invariants for effective stress and deviatoric stress, p and q. The first invariant, effective pressure stress, p, is defined as

$$p = -\frac{1}{3} trace(\bar{\sigma}) = -\frac{1}{3} I_1 \tag{1}$$

where $I_1 = trace\,(\bar{\sigma})$ and $\bar{\sigma}$ is the stress tensor (the overscore denotes matrix). For a triaxial test, $\sigma_2 = \sigma_3$ and eq 1 can be reduced to

$$p = -\left(\frac{\sigma_1 + 2\sigma_3}{3} \right). \tag{2}$$

The invariant used by ABAQUS, q, is the deviatoric stress defined as

$$q = \sqrt{\frac{3}{2} \bar{S} : \bar{S}} \tag{3}$$

where "**:**" denotes the scalar product and

$$\bar{S} = \bar{\sigma} + p\bar{I} \tag{4}$$

where $\bar{I}$ is the identity matrix. For a triaxial stress state, eq 4 is reduced to the expression for deviatoric stress:

$$q = \sigma_1 - \sigma_3 \tag{5}$$

where σ_1 is the total major stress and σ_3 is the radial stress or confining pressure.

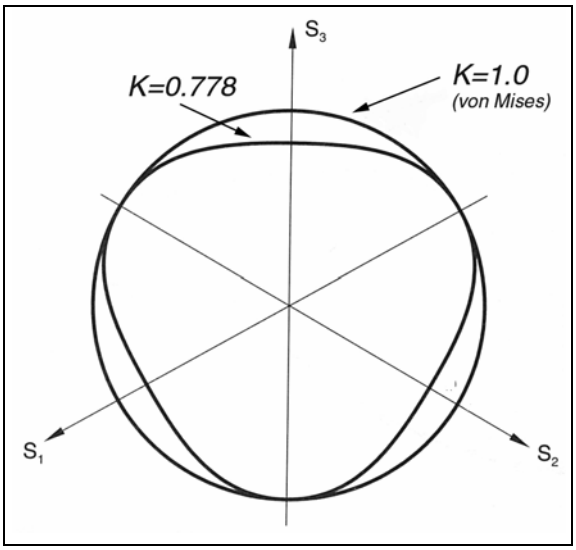

Figure 2. Modified Drucker–Prager yield surface in deviatoric space. (After HKS 2002.)

For the modified CDP model used in this study, the yield surface is a modified von Mises yield surface (i.e., the material constant $K = 1.0$), which is circular in the deviatoric plane (Fig. 2). In the p–q plane the yield surface has two major segments: the Drucker–Prager portion of the curve (analogous to the Mohr–Coulomb line) defines shear deformation, and the cap portion of the surface defines the intersection with the pressure axis and compressive deformation, shown in Figure 3. The following equations define the yield criteria in each section of the yield surface.

For the Drucker–Prager shear or distortional failure

$$F_s = q - p\tan\beta - d = 0\,. \tag{6}$$

where d is material cohesion and β is material angle of friction.

For the cap region of compactive–dilatant failure

$$F_c = \sqrt{\left(p - p_a\right)^2 + \left[\frac{Rq}{\left(1 + \alpha - \alpha/\cos\beta\right)}\right]^2} - R\left(d + p_a\tan\beta\right) = 0 \tag{7}$$

where α is a transition parameter, ranging typically from 0.0 to 0.05, that smoothes the transition between the shear failure and the cap failure; R is a

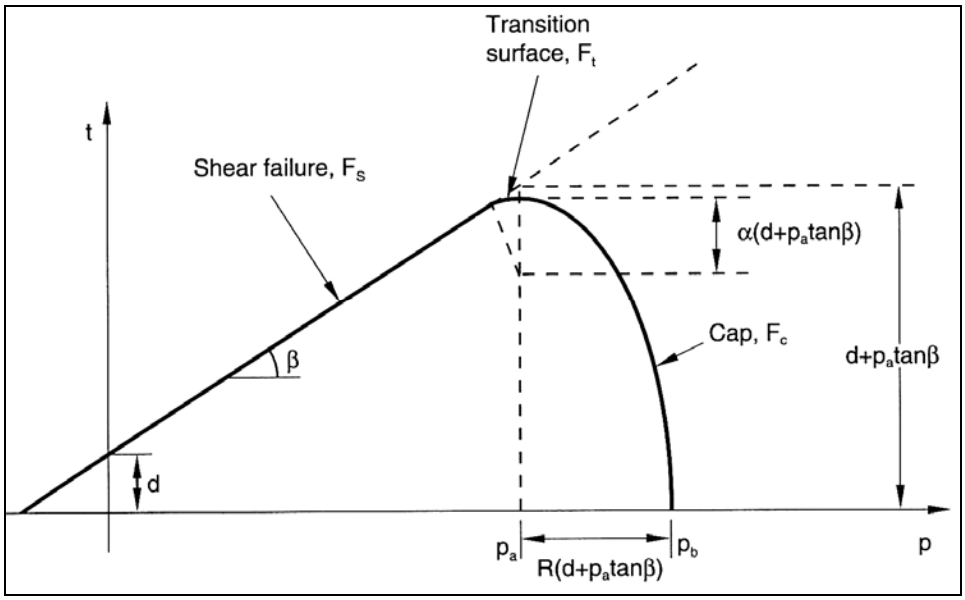

Figure 3. Modified Capped Drucker–Prager yield surface in the *p–t* plane. (After HKS 2002.)

material parameter controlling the cap eccentricity; and p_a defines the evolution of the cap along the pressure axes (via p_b–ε_{vol} hardening law) according to

$$R = \frac{\sqrt{(p_b - p_a^2) - q_a{}^2}}{p_b - p_a} \tag{8}$$

$$p_a = \frac{p_b - Rd}{(1 + R\tan\beta)}. \tag{9}$$

The transition between the shear and the cap failure is:

$$F_t = \sqrt{(p - p_a)^2 + \left[q - \left(1 - \frac{\alpha}{\cos\beta}\right)(d + p_a\tan\beta)\right]^2} - \alpha(d + p_a\tan\beta) = 0 \tag{10}$$

The pressure–volume relationships define both hardening and softening through volume changes based on how the cap portion of the yield surfaces expands and contracts. The hardening of the cap can be defined as an exponential relationship

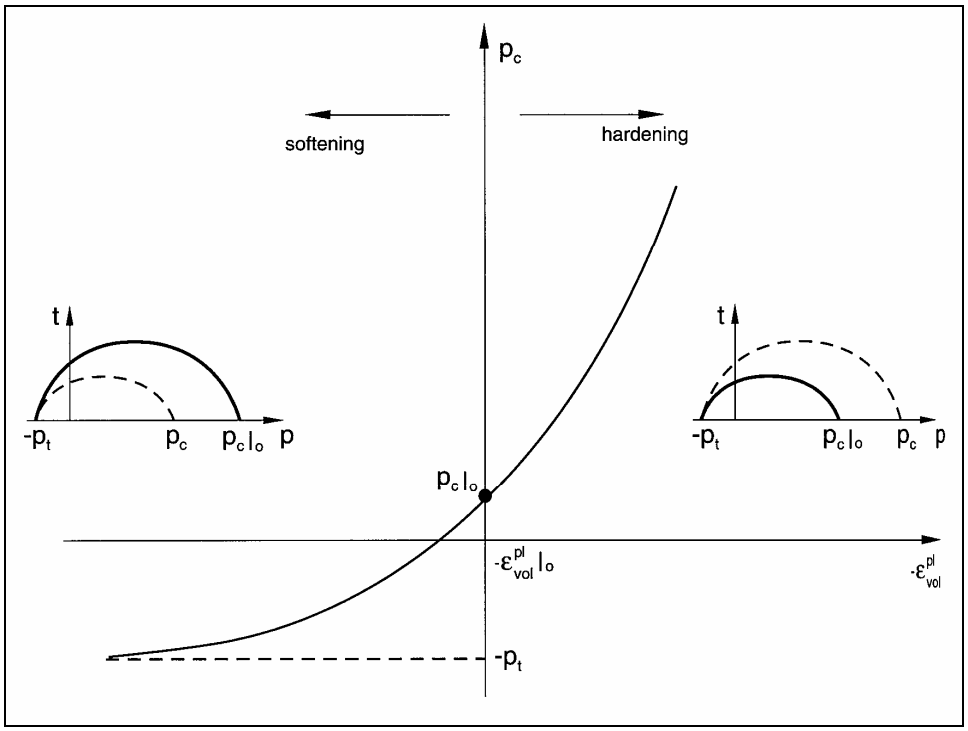

Figure 4. Cap contraction or expansion reflecting the softening (left) or hardening (right) of the material. (After HKS 2002.)

in the pressure–volume space as shown in Figure 4, or it is entered in a piecewise fashion as a table of p_b and ε_{vol}^{pl} pairs. The piecewise approach is recommended by HKS (2002) for a better fit to the data and better model performance.

The main elements of the modified CDP model are illustrated in Figures 3 and 4.

The plastic flow is defined by an elliptical potential surface as shown in Figure 5. Flow is associative (normal to the surface) in the cap region; therefore, the equation for the flow surface is identical to the equation for the cap yield surface. In the transition and shear region, the flow is non-associative (flow potential is independent of the failure surface) and is defined by the following equation for the flow potential:

$$G_s = \sqrt{\left[\left(p_a - p\right)\tan\beta\right]^2 + \left[\frac{q}{1+\alpha-\alpha/\cos\beta}\right]^2} \tag{11}$$

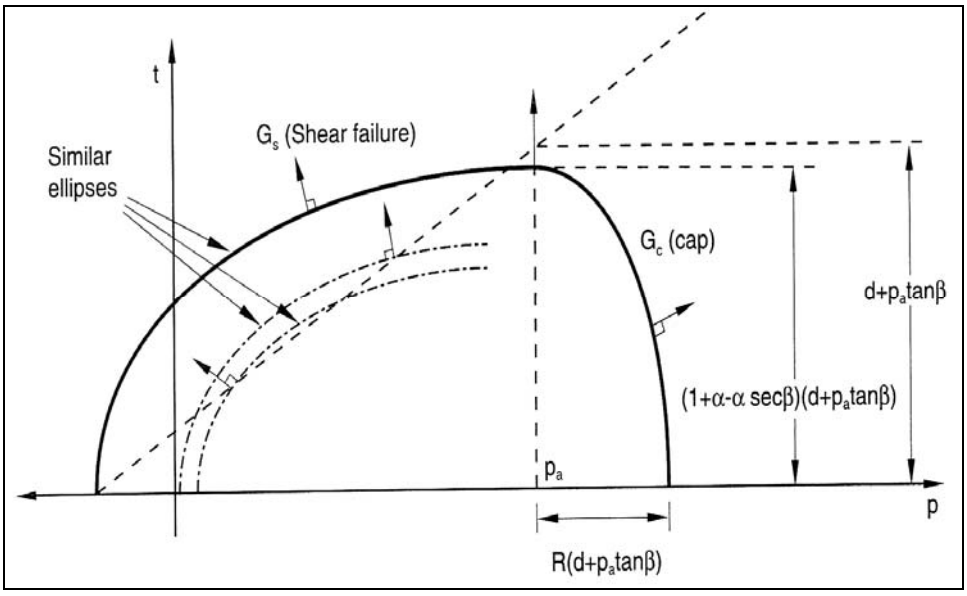

Figure 5. Modified CDP flow potential in the *p–q* plane. (After HKS 2002.)

The elastic strains are estimated with material parameters λ and κ, slopes of the loading (compression) and unloading (elastic) portion of the curve, respectively, E = Young's modulus, and ν = Poisson's ratio.

Soil Material

Triaxial compression tests were performed on Lebanon Sand. This a highly frost-susceptible material according to laboratory frost heave tests documented in Shoop (1988), is classified as silty sand (SM) using the Unified Soil Classification System (USCS), and exhibits thaw weakening in pavement structures. This soil would represent a spring off-road, trail, or subgrade material or a poor unsurfaced road material in the northeastern United States. The soil was used in full-scale tests of paved and unpaved test sections in the CRREL Frost Effects Research Facility (FERF). The material grain size distribution is shown in Figure 6. The soil is non-plastic (PI = 0) and has a maximum density of 1826 kg/m^3 (114 pcf) at an optimum moisture content of 13% (ASTM D 1557 Modified Proctor Test, Figure 7). This soil is characterized for moisture migration during freeze–thaw in Shoop and Bigl (1997), for frost heave in Shoop and Henry (1991), for in-situ shear strength in Shoop (1993), and for triaxial testing on frozen cores in Shoop (1988). The pertinent background data for Lebanon Sand is included in Appendix A. Soil strength results from California Bearing Ratio (CBR) tests at various moisture contents are shown in Figure 8 (Shoop 1988).

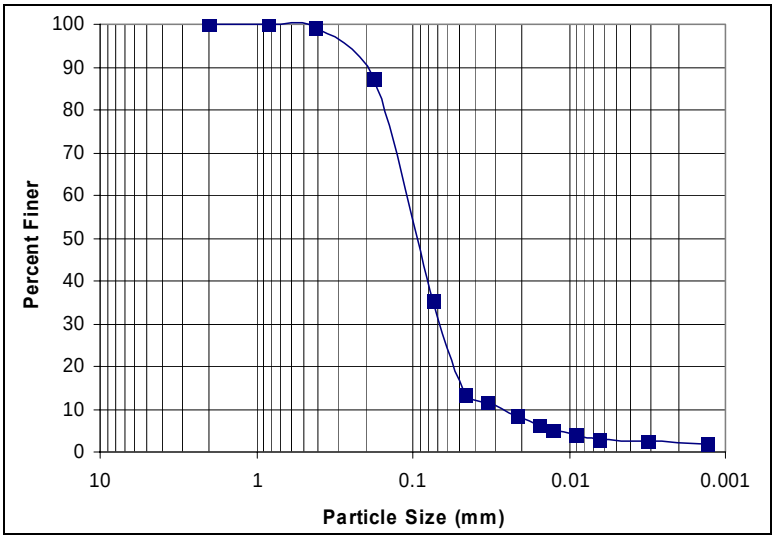

Figure 6. Lebanon Sand grain size analysis, with D_{10} = 0.027, C_u = 4.579.

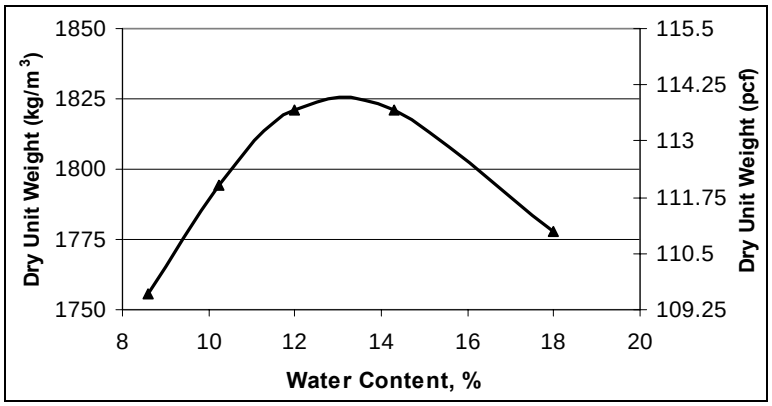

Figure 7. Compaction curve, with maximum density = 1826 kg/m^3 (114 lb/ft^3) and optimum moisture content = 13%.

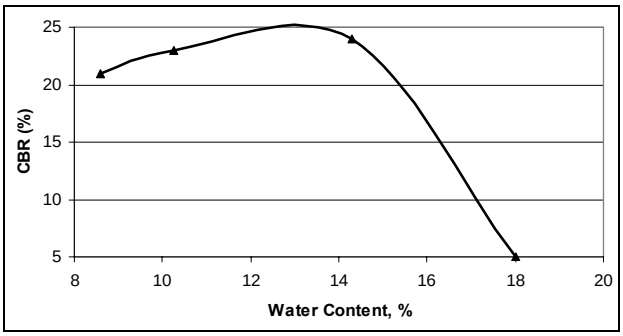

Figure 8. Soil strength from California Bearing Ratio (CBR) tests at various moisture contents.

Sample Preparation and Triaxial Test Procedures

The tests performed on this soil included saturated triaxial tests and unsaturated triaxial tests at specific moisture and density conditions experienced during the freeze–thaw testing in FERF; the average moisture content was 13% (wet of optimum) and the average dry density was 1760 kg/m^3 (110 pcf). Standard triaxial test specimens (2.8 in. in diameter and 5.5 in. high) were fabricated. The initial and test conditions (moisture and density) for each of the samples are given in Appendix B.

All specimens were molded using twelve equal lifts of soil. Sufficient water was mixed with the air-dried soil to increase the water content of each lift. After each lift was placed in the mold, a handheld rammer was used to compact the soil to a specified thickness. The mold was then placed on the base of the triaxial chamber and placed under a vacuum of about 35 kPa (5 psi). After the vacuum had stabilized and it was determined that the membrane was not leaking, the mold was removed from the specimen, and the dimensions of the membrane-encapsulated specimen were recorded. The triaxial chamber was then assembled.

The vacuum applied to the specimen through the pore pressure system was then gradually reduced as the chamber pressure was simultaneously increased to the desired consolidation pressure. The sample was then back-pressure saturated, maintaining the test effective stress until a minimum Skemptom's pore pressure parameter (B) value of 0.95 was obtained (a reasonable value for sands). This usually took about a day and resulted in a fully saturated sample (saturation at or near 100%).

Once the B-value had been achieved, the closed-loop hydraulic system was activated, and the (axial) load cell was attached to the specimen's top platen. Initial instrumentation readings, i.e., chamber pressure, pore pressure, axial load, and axial deformation using the "closed-loop" LVDT (linear variable differential transformer) and the "specimen" LVDT, were recorded. A deformation (or displacement) rate-controlled shear test was conducted. The rate of strain was about 1% per minute. Following the completion of each test, the specimen was removed from the triaxial chamber and dried in an oven at 110°C to obtain the post-test water content and dry weight of soil.

Two types of saturated triaxial tests were conducted: 1) back-pressure saturated, consolidated, undrained triaxial shear tests with pore pressure measurements ($\overline{R}$), also known as $\overline{CU}$ (Confined Undrained back-pressure saturated), and 2) back-pressure saturated, consolidated, drained triaxial shear tests (S) without pore pressure measurements. In general the procedures outlined in EM (Engineer Manual) 1110-2-1906 (U.S. Army COE 1970) were followed for both tests.

3 TEST RESULTS AND MATERIAL PROPERTY DETERMINATION

Saturated Triaxial Tests: Drained Shear Result for Lebanon Sand

Drained shear tests were performed using three nominal confining pressures: 14, 28, and 40 kPa (2, 4, and 6 psi) and two repetitions of each condition. The low confining pressures were chosen to simulate the near-surface conditions (for a thawing off-road or trail surface). Each test was performed on a 7-cm- (2.8-in.-) diameter by 14-cm- (5.5-in.-) high sample, which was back-pressure saturated and consolidated. The samples were prepared to initial conditions of 9% water content, approximately 1730 kg/m^3 (108 pcf) dry density (compaction ratio of 93%), and 0.53 void ratio. The water content of the specimens after saturation ranged from 17.5 to 17.8%. Five of these tests are used in the following analyses and summarized in Table 1. Test results are shown in the two graphs in Figure 9 as deviatoric stress, q, vs. axial strain, ε_{ax}, and volumetric strain vs. axial strain.

The shear failure envelope is obtained by plotting the data in p–q space and joining the yield points of the stress paths of each of the tests, as shown in Figure 10.

An alternate method of calculating the Drucker–Prager cohesion, d and β, is to use the following equations based on Mohr–Coulomb parameters:

$$\tan \beta = 1.73 \sin\phi \tag{12}$$

$$d = c1.73 \cos\phi. \tag{13}$$

Table 1. Summary of Lebanon Sand drained shear data.

Test no.	Average σ_3 (kPa)	Peak deviatoric stress, q (kPa)	Corresponding strain	Max. mean stress, p (kPa)	Initial void ratio	Max. volumetric strain
2DS1	14	42	0.18	28	0.53	0.029
2DS2	15	41	0.24	29	0.54	0.028
4DS2	28	76	0.16	52	0.53	0.032
6DS1	43	133	0.19	88	0.54	0.038
6DS2	39	107	0.20	76	0.54	0.039

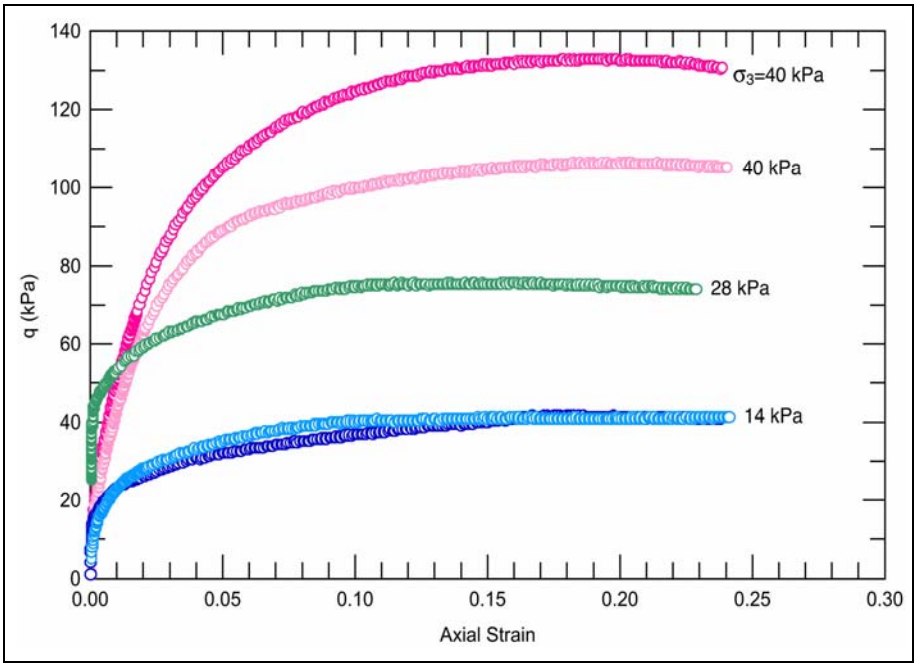

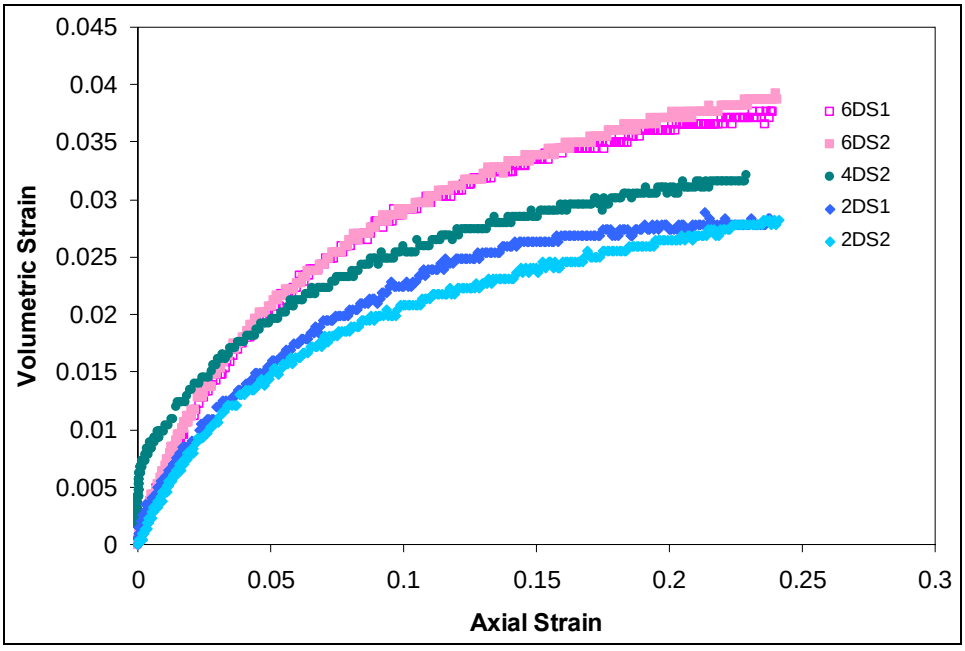

Figure 9. Drained triaxial tests.

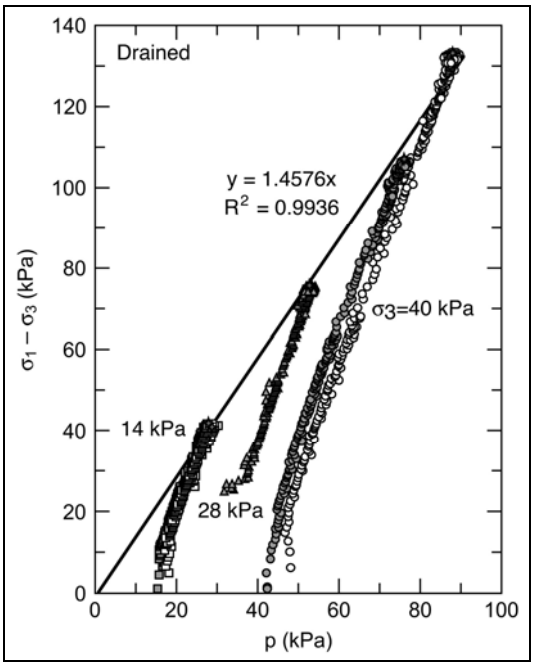

Figure 10. Shear failure line for Lebanon Sand drained shear tests, d = 0, β = 55.6°.

The Mohr–Coulomb analysis of these tests is shown in Figure 11. A failure line drawn tangent to the failure circles, defined by eq 14, results in a cohesion value of c = 0 kPa and a friction angle of ϕ = 36°.

$$\tau = c + \sigma \tan \phi \,. \tag{14}$$

Unfortunately this test series did not include unloading and reloading the sample, so the elastic properties were obtained by taking the initial slope of the stress–strain curve. Young's modulus, E, for the drained shear tests is found to be 17253 kPa. A Poisson's ratio, v, of 0.32 is found by plotting radial strain with axial strain. It should be noted that the Young's modulus from the initial loading portion may be off by a factor of two when compared with that obtained from unloading–reloading data (although repeatability in resilient modulus testing is of the same order of magnitude). This may not be critical in our case as we anticipate the elastic strains to be insignificant compared to the plastic strains.

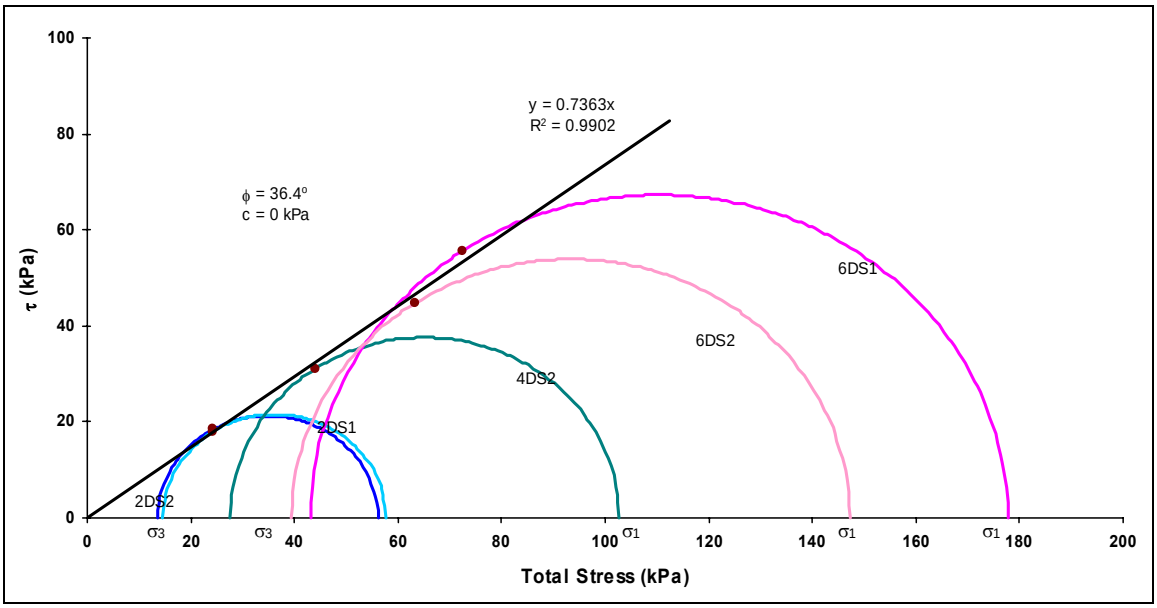

Figure 11. Mohr circle analysis for drained triaxial tests, *c* = 0 kPa, ϕ = 36°.

Saturated Triaxial Tests: Undrained Shear Result for Lebanon Sand

Undrained shear tests, with pore pressure measurements, for Lebanon Sand material were also performed with three confining pressures: 14, 28, and 40 kPa (2, 4, and 6 psi) and three test repetitions. The specimens were molded into a 7-cm- (2.8-in.-) diameter by 14-cm- (5.5-in.-) high sample, then back-pressure saturated and consolidated. The initial sample conditions were 9% water content and approximately 1730 kg/m^3 (108 pcf) dry density. Five of these tests are used in the following analyses and are summarized in Table 2. A graph of deviatoric stress against axial strain of the test data is shown in Figure 12. Pore pressure measurements are shown in Figure 13.

Table 2. Summary of Lebanon Sand undrained shear data.

Test no.	Average σ_3 (confining pressure) (kPa)	Peak q ($\sigma_3 - \sigma_3$) (kPa)	Corresponding			Initial void ratio, e
			σ'_3 (kPa)	σ'_1 (kPa)	p' (kPa)	
2US3	13	25	9	35	22	0.52
4US2	28	21	13	34	24	0.51
4US3	26	20	10	30	20	0.53
6US2	40	26	17	45	31	0.53
6US3	40	27	17	44	31	0.50

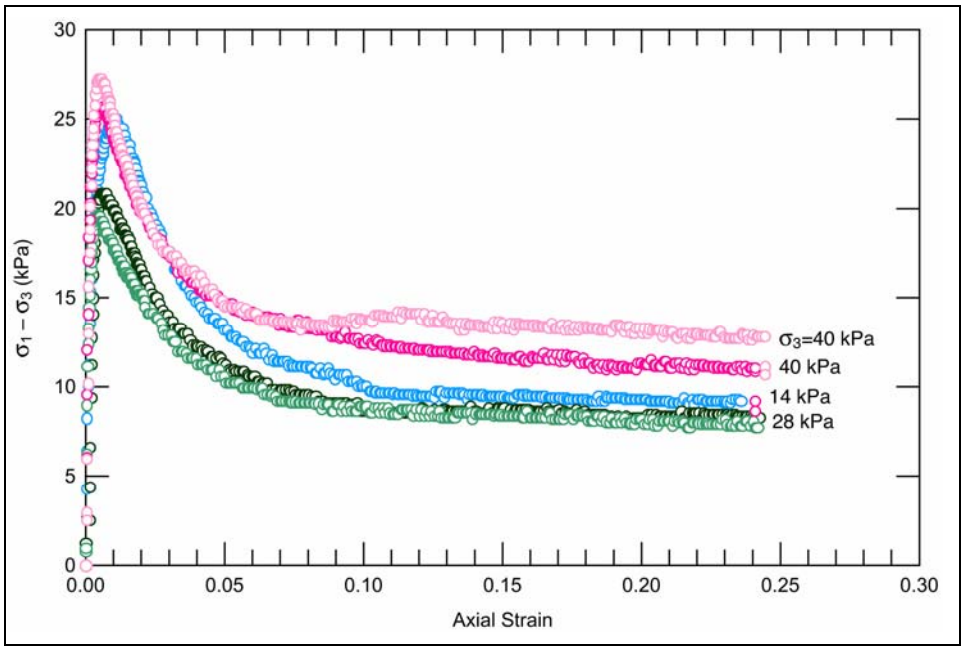

Figure 12. Consolidated, undrained triaxial tests.

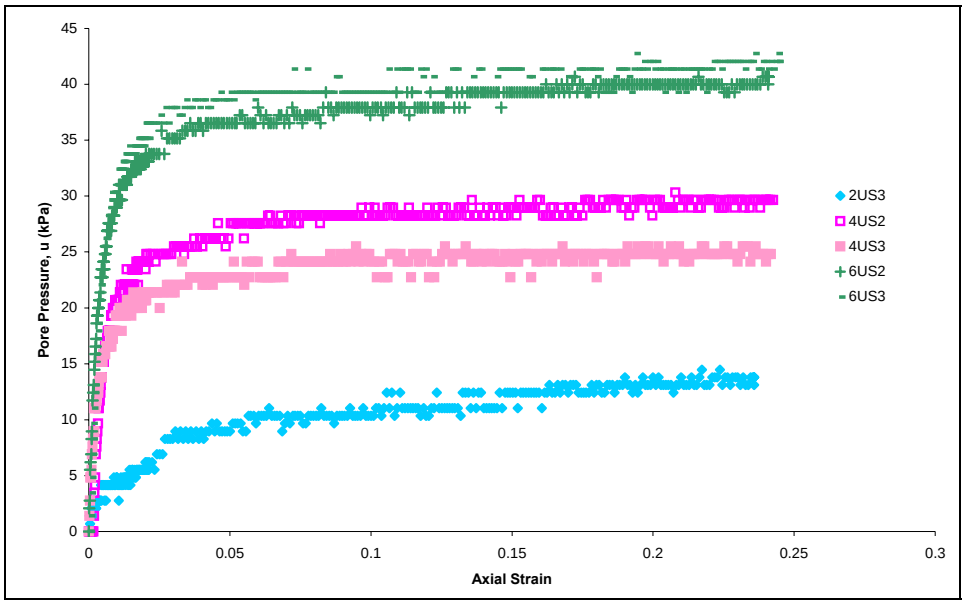

Figure 13. Undrained triaxial tests pore pressure measurements.

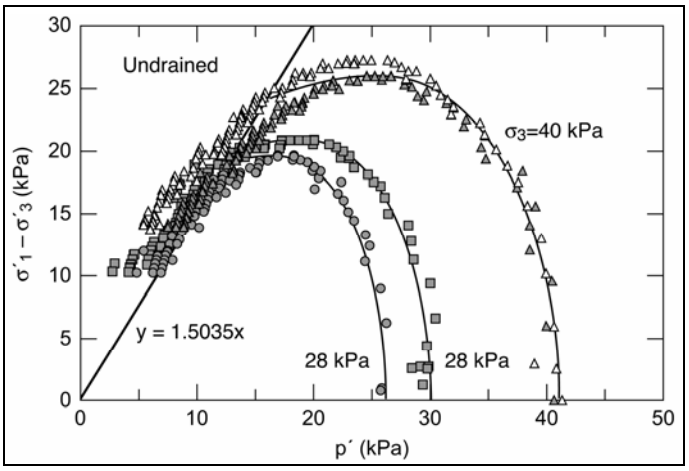

Figure 14. Stress paths for undrained shear tests, *d* = 0, β = 56.4°.

The stress paths from each test, in p'–q' space, are shown in Figure 14. As with the drained data, the critical state analysis for undrained shear data was derived from eq 2 and 5 using the effective stresses. A compilation of the test data for the saturated conditions is given in Figure 15 and shows the good agreement among the tests.

The Mohr's circle analysis of these tests is shown in Figure 16. A failure line is drawn tangent to the remaining four failure circles having a cohesion value of c = 4.8 kPa and a friction angle of ϕ = 17° for effective stress, and c = 12.1 kPa and ϕ = 0° for total stress.

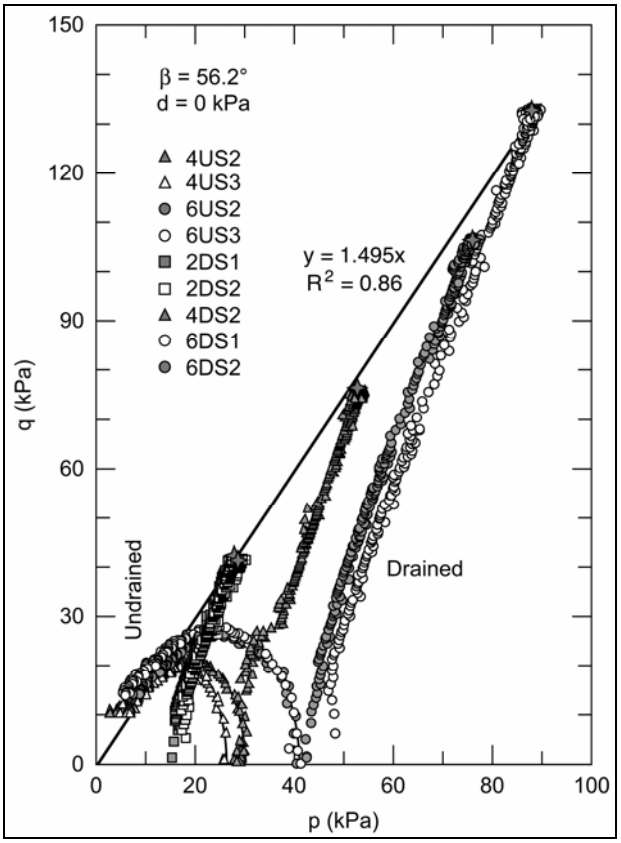

Figure 15. Test data for all of the saturated triaxial tests (drained and undrained).

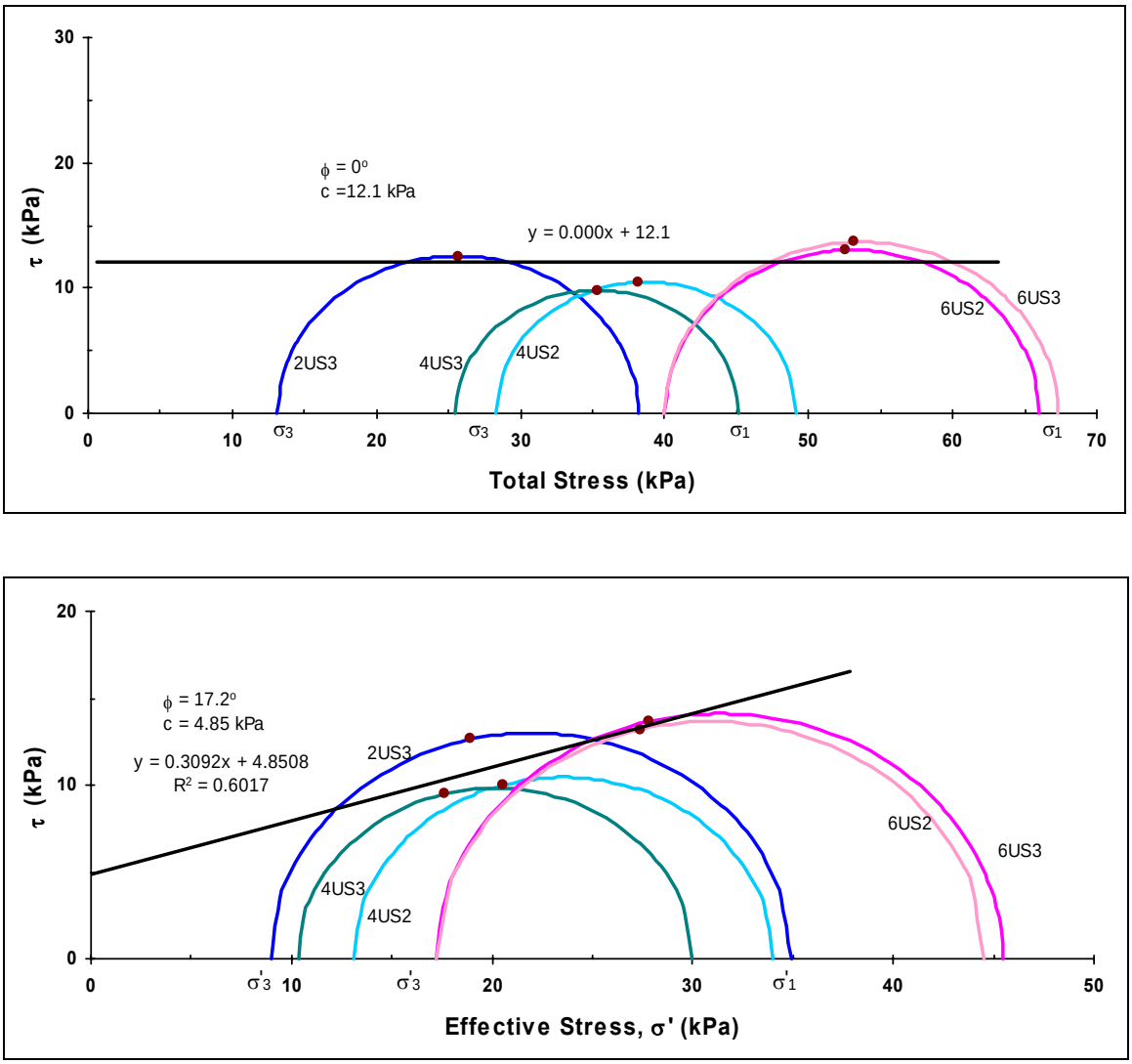

Figure 16. Mohr circle analysis for undrained triaxial tests; *c* = 12.1 kPa and ϕ = 0° for total stress (top), and *c* = 4.8 kPa and ϕ = 17° for effective stress (bottom).

Hydrostatic Consolidation Test

Hydrostatic consolidation tests were performed to determine the pressure–volume relationship of the material. The test results are shown graphically in Figure 17 and are compared to a similar sand in a compacted state in Figure 18.

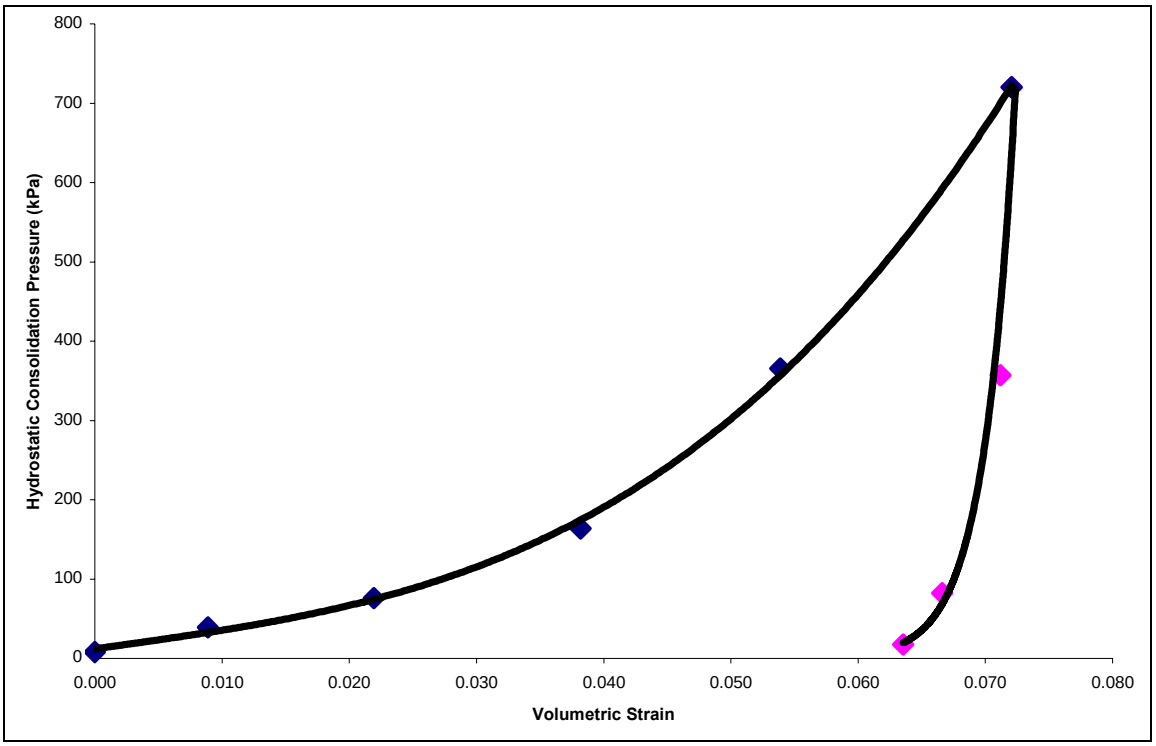

Figure 17. Hydrostatic compression vs. volumetric strain.

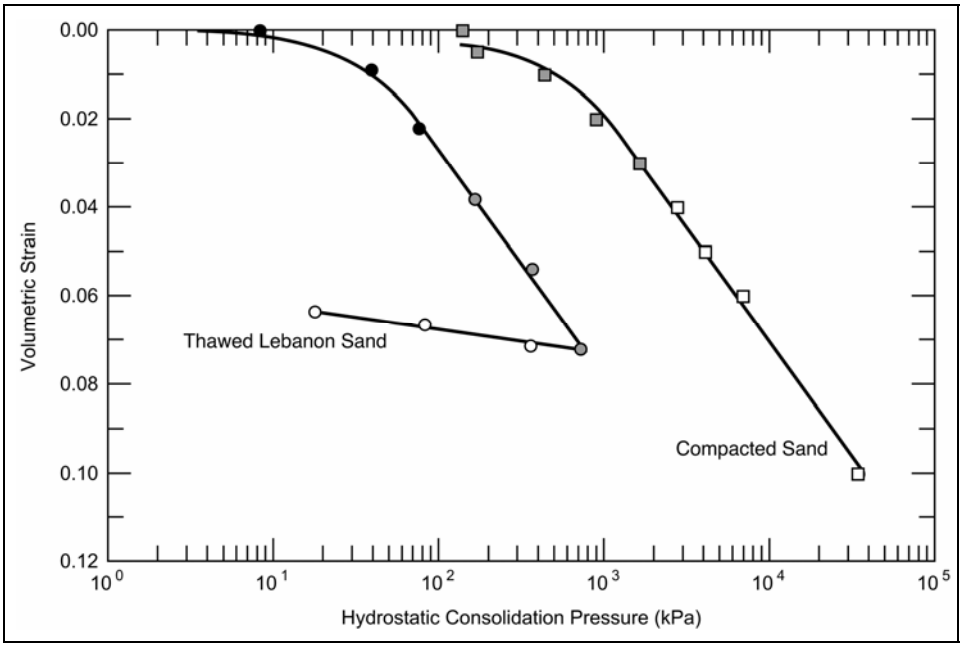

Figure 18. Pressure–volume relationship of Lebanon Sand compared to compacted sand.

The pressure–volume relationship can also be input directly in tabular form. The latter is suggested as more accurate (HKS 2002) and was used in this study (Table 3).

Table 3. Hardening model for Lebanon Sand.

Hydrostatic stress, P_b MPa (psi)	Volumetric plastic strain
0.0082 (1.2)	0
0.0389 (5.6)	0.009
0.0760 (11.0)	0.022
0.1639 (23.8)	0.038
0.3655 (53.0)	0.054
0.7201 (104.4)	0.072
Unloading	**Volumetric strain**
0.3569 (51.8)	0.071
0.0822 (11.9)	0.067
0.0178 (2.6)	0.064

Constant Water Content Tests at Specific Thawing Conditions

Several triaxial tests, without pore pressure measurements, were performed on Lebanon Sand at an average dry density of 1760 kg/m^3 (110 pcf) and moisture content of 13% (68% of saturation). A brief summary of the results are presented here. Additional analysis and a more detailed report on these tests are forthcoming. The specimens were molded into a 7-cm- (2.8-in.-) diameter by 15-cm- (6-in.-) high cylinders in five equal lifts. The confining pressures used were 14, 28, and 40 kPa (2, 4, and 6 psi). Each test was subjected to loading and unloading cycles as shown in Figure 19. Table 4 summarizes the test analysis.

Table 4. Summary of Lebanon Sand undrained shear tests for samples at 13% moisture content.

Test no.	Average σ_3 (confining pressure) (kPa)	Peak q ($\sigma_1 - \sigma_3$) (kPa)	Max. mean stress, p (kPa)
2.1	14	57	33
2.3	14	61	34
2.4	14	86	43
2.5	14	101	47
4.2	27	83	55
6.1	41	159	94
6.2	42	121	82

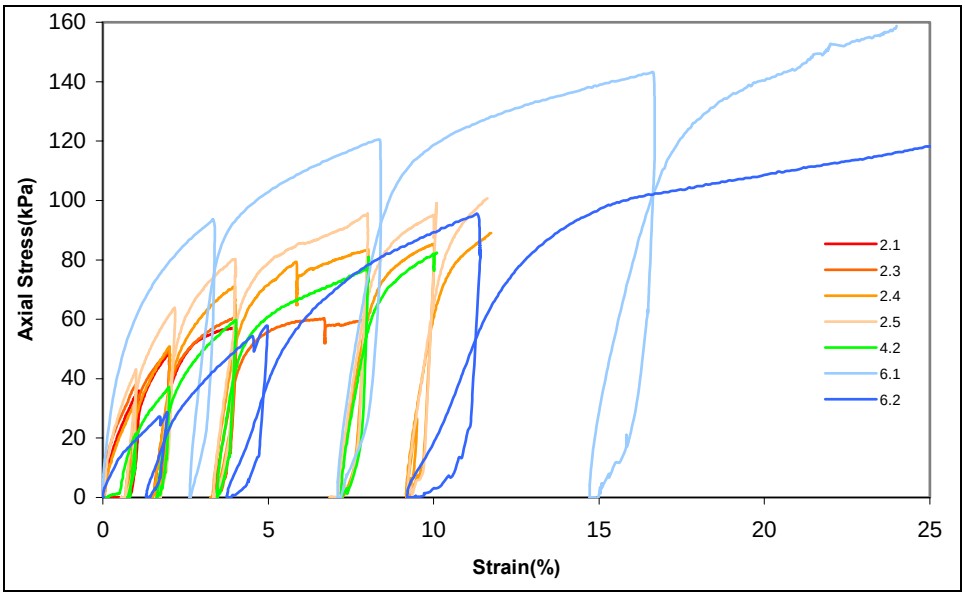

Figure 19. Triaxial, undrained shear data for samples representing specific thawing conditions of an average moisture content of 13% and a dry density of 1760 kg/m^3. Legend indicates test number from Table 4 and confining pressure in psi.

The *p*–*q* yield analyses resulted in d = 16.7 kPa, β = 54.8° (Fig. 20). These tests show some cohesion value, or apparent cohesion, as is often the case in unsaturated, moist soil.

The Mohr's circle analysis is given in Figure 21. The resulting c and φ values are very similar to those obtained from the saturated, drained tests.

A Young's modulus value of 8490 kPa was obtained by averaging all of the values taken from the stress vs. strain graphs of each laboratory test. The slope of each loading curve was measured and then

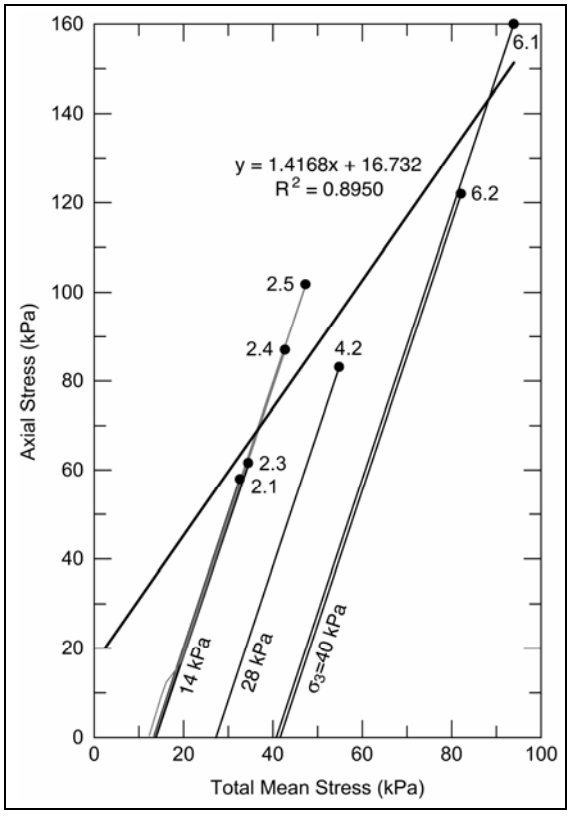

Figure 20. Shear failure line for samples at 13% moisture content, d = 16.7 kPa, β = 54.8°.

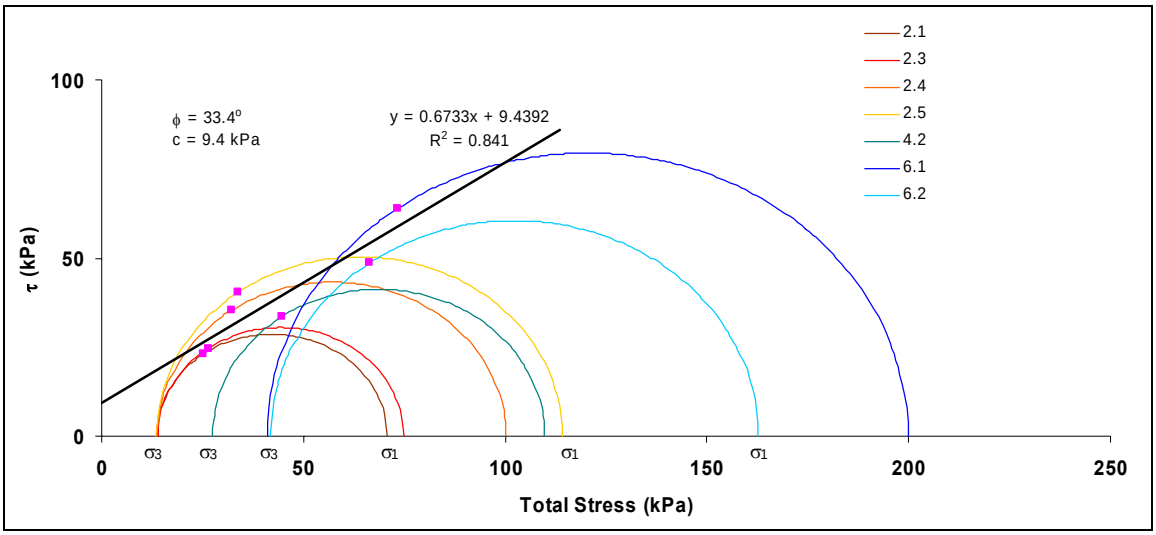

Figure 21. Mohr's circle analysis for samples at 13% moisture content; *c* = 9.4 kPa, ϕ = 33°.

averaged with the other loading curves for that specific graph. An average was found for each confining pressure [14, 28, and 40 kPa (2, 4, and 6 psi)] and then a final Young's modulus of 8490 kPa (1230 psi) was calculated. Graphs of the test data and a table of the calculations are given in Appendix C.

A summary of the shear failure line parameters obtained using the Mohr–Coulomb analysis and eq 12 and 13 are given in Table 5. In Table 5, *d* ranges from 0 to 13 kPa, and β ranges from 27 to 45º. These are somewhat lower than the values from the *p*–*q* plots and were not used for the remainder of the study.

Table 5. Shear line parameters from Mohr–Coulomb analysis.

	c **(kPa)**	***d*** **(kPa)**	**ϕ (°)**	**β (°)**
Drained, saturated	0	0	36	45
Undrained, saturated	4.8	8	17	27
Undrained, 13% mc	9.0	13	33	44

Summary of Test Data

Table 6 summarizes the material parameters from all of the test data. In general, the constitutive model parameters shown in Table 6 reflect the specific test conditions. The final model parameters chosen to represent the thawing soil

behavior were a combination of the parameters obtained from the different test conditions. The Young's modulus values from the loading–reloading curve were about half of those from the initial loading of the saturated triaxial tests. As most of the deformation is plastic, the value of Young's modulus does not have a huge influence on the results, and the value from the unsaturated samples was chosen to represent the soil in the final model parameters. The other parameter that was significantly between the saturated tests and the tests at 13% moisture content is the cohesion. Both of the saturated test conditions show essentially no cohesion, as would be expected for saturated, sandy soil. The samples tested at 13% moisture content show a small amount of cohesion, or apparent cohesion, as is typical in unsaturated soils because of moisture tension. A value between these two extremes was chosen to represent the overall thawing soil behavior in the final constitutive model. The remaining parameters were within the range of the tests and were refined to obtain the best response in model simulations as discussed in the following section.

The β values appear high, but they are based on the ABAQUS formulation of the deviatoric stress invariant *q* and agree with values reported by Arnold (2002). Using a Mohr–Coulomb approach, the angle of internal friction φ for these tests is 36° and 17° for saturated drained and undrained tests, respectively, and 33° for the tests at 13% moisture content; these values are reasonable for sands.

Table 6. Material constants comparison for the Capped Drucker–Prager model on Lebanon Sand.

Material parameter	Saturated drained shear	Saturated undrained shear	Shear at 13% moisture content	Final model parameters
E, Young's modulus (kPa)	17,250	17,440	8,490	8500
v, Poisson's ratio	0.32	0.5	—	0.32
β, Drucker–Prager angle of friction (degrees)	55.6	56.4	54.8	55.8
d, Drucker–Prager material cohesion (kPa)	0	0	16.7	10.0
R, cap eccentricity		0.15–0.88		0.45
Initial value of volumetric plastic strain		0.001		0
K, flow stress ratio		1.0		1.0

4 SIMULATION OF LABORATORY TESTING

The material properties generated from laboratory testing (Table 6) were used to create a working simulation of the triaxial load tests by manipulating the parameters of the material model to ensure a good fit for a wide range of simulated test parameters. After a good fit to the triaxial test data was obtained, the material model was used in a 3-D simulation of an unpaved road. Some additional adjustments to the material model were needed, primarily to account for apparent cohesion in the unconfined road surface. Although the best-fit parameters to the saturated triaxial test data included very low values of CDP cohesion ($d \approx 0$), this resulted in immediate dilatant failure of the surface elements as the wheel was applied to the soil. Arguably this surface layer is likely not saturated and some apparent cohesion would be present (as in the 13% moisture content test results), so some cohesion was included in the final constitutive model parameters.

A final set of parameters was obtained that gave a reasonable fit to both lab and field observations. These parameters are listed in the last column of Table 6. The final material model parameters are compared to the laboratory data in Figure 22. The model captures the stiffness of the higher confining pressure better than that of the low confining pressure.

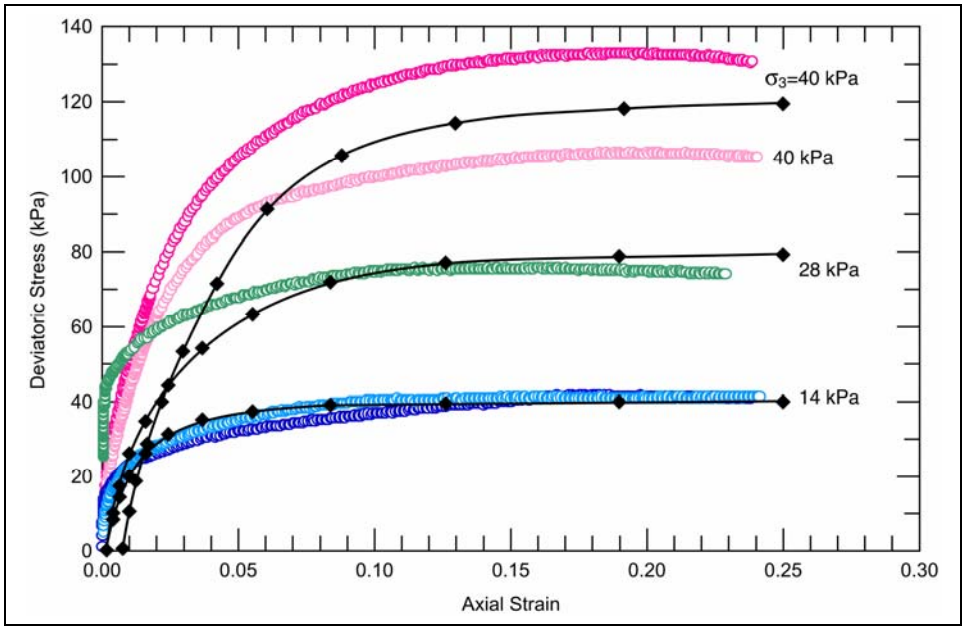

Figure 22. Comparison of final model parameters (Table 6) with laboratory data for 14, 28, and 40 kPa confining pressure.

5 VALIDATION AND APPLICATION

Finite element simulations of experiments performed on Lebanon Sand were used to validate the material model and assure that it was robust under a variety of loading and simulation conditions. Three finite element simulations were constructed; details of these finite element simulations are given elsewhere. For completeness of this report, brief descriptions of each simulation are listed below.

- Direct shear tests were performed on thawing Lebanon Sand samples taken from the FERF test sections. The experimental data for the direct shear tests are summarized in Shoop (1993). Tests were completed at six values of normal loading. The mesh for the simulations is shown in Figure 23a. The simulations modeled the data very well except for very small normal loads, as shown in Figure 24 (Haehnel and Shoop, in prep.).
- Various finite element models were generated to simulate vehicle travel on an unpaved road or trail or an off-road condition. These models were implemented in a three-dimensional dynamic analysis with a wheel rolling over the soil. Simulations of the unpaved road were used to study the effects of vehicle speed, load, suspension system, wheel torque, wheel slip, etc., on the deterioration of unsurfaced roads or trails in terms of rutting and washboard formation (Shoop et al. 2002). One of the meshes for this study is shown in Figure 23b. Qualitatively the results from the finite element model agree with observations of rutting and approximate resisting forces on the wheel. Both the simulation and field observations indicate moderate plowing and flowing of the soil to the sides and in front of the wheel and the wheel sinking through the full depth of the thawed soil layer such that the wheel is nearly rolling on the top of the frozen layer.
- The final study was for a layered pavement system (Fig. 23c). This model will be used with varying pavement structures and frost–thaw depths to study the impact of different vehicle loading and frost–thaw layering on the pavement deformation. This type of model will also be used to study airfield structures for unpaved and marginal airfields during thaw or for paved airfields with thawing subgrades.

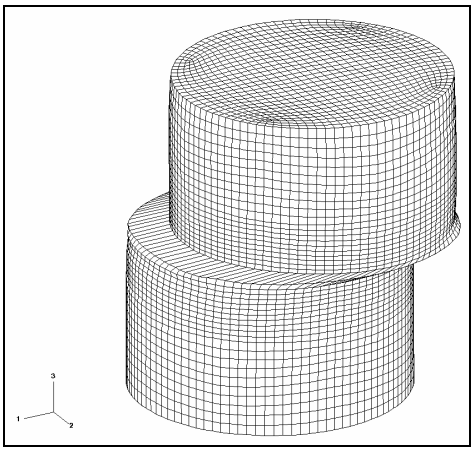

a. Direct shear test.

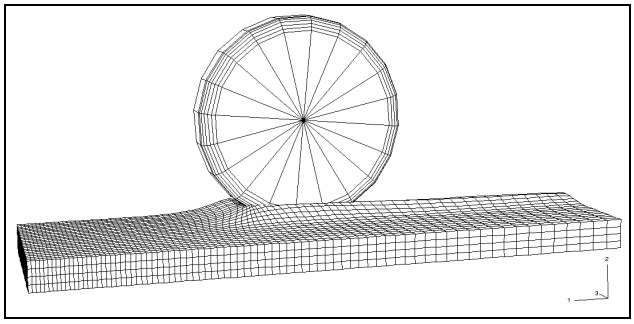

b. Wheel rolling on thawing soil.

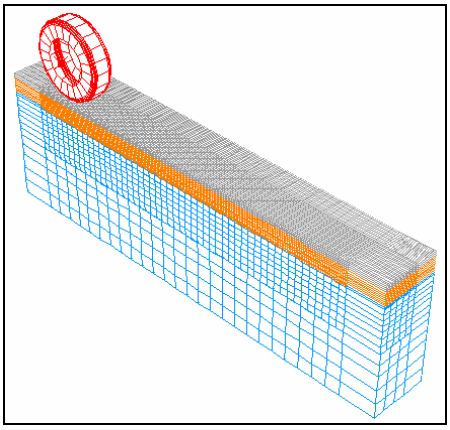

c. Layered pavement system.

Figure 23. Three-dimensional finite element simulations, all incorporating the Lebanon Sand thawing soil material model.

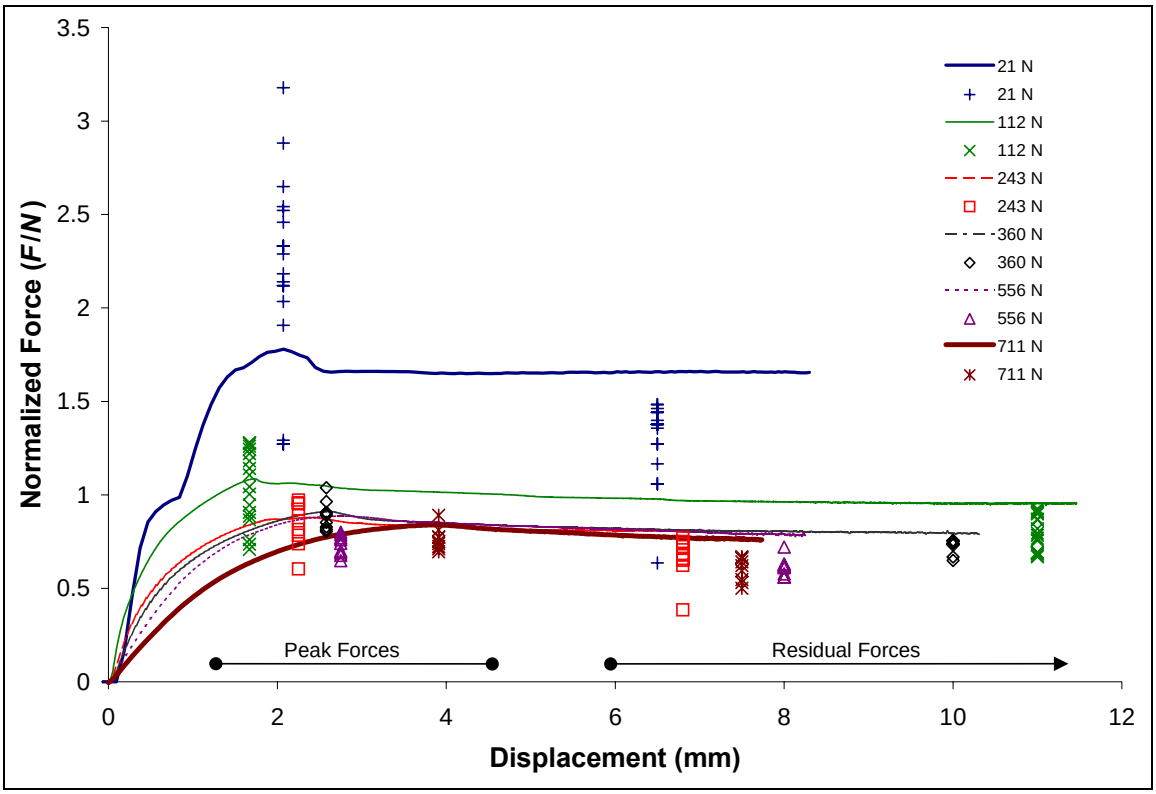

Figure 24. Comparison of finite element simulations of the direct shear test with laboratory data.

6 THAWING SOIL MODEL COMPARED TO OTHER GRANULAR MATERIALS

The CDP model for Lebanon Sand is compared to some other granular materials in Table 7. The McCormick Ranch Sand (HKS 1996, DiMaggio and Sandler 1971, 1976) and the Lebanon Sand are fairly similar in grain size, while the A-4 soil (Burton et al. 2003) is a silt (ML). The grain size distributions are plotted in Figure 25.

Figure 26 compares the hardening curves for the materials. Although the McCormick Ranch Sand has a grain size distribution similar to that of Lebanon Sand, the McCormick Sand was tested in a much more compacted state and at higher pressures (for a much different application). Also, the A-4 soil samples were prepared at optimum moisture and density, not the loose conditions of the thawing Lebanon Sand. Therefore, both other soils required higher pressures than Lebanon Sand for the same volumetric strain.

For contrast, a fresh snow material model from Shoop (2001) was also included. The compaction of snow is an order of magnitude greater than for soils, as can be seen by the scale for volumetric strain of 0 to 1.6 for snow and 0 to 0.1 for the soils (Fig. 26).

Table 7. Material constants for Capped Drucker–Prager model for various materials.

Material parameter	A-4* saturated drained shear	McCormick Ranch Sand† saturated drained shear	Snow** (SNOW2)	Lebanon Sand final
E, Young's modulus, kPa	16,000	689,475	1,379	8,500
v, Poisson's ratio	0.33	0.25	0.3	0.32
β, Drucker–Prager angle of friction	53°	14.6	22.5	55.8
d, Drucker–Prager material cohesion, kPa	16.6	1190	15	10
R, cap eccentricity	0.45	0.1	1.1e-4	0.45
$\varepsilon_{vol}^{pl}\|_0$, initial value of volumetric plastic strain	0.001	0.001	0.001	0
K, flow stress ratio	1.0	1.0	1.0	1.0

* Burton et al. (2003)

† HKS (1996), DiMaggio and Sandler (1971, 1976)

** Shoop et al. (1999), Shoop (2001)

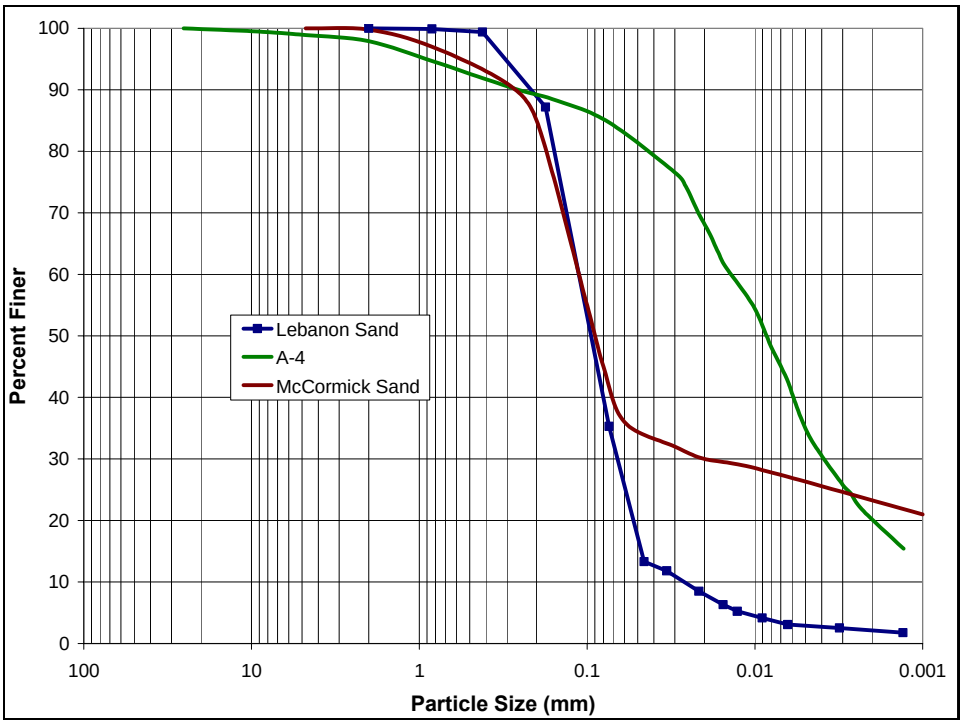

Figure 25. Lebanon Sand grain size analysis, D_{10} = 0.027, C_u = 4.579, compared with the McCormick Sand and A-4 silt.

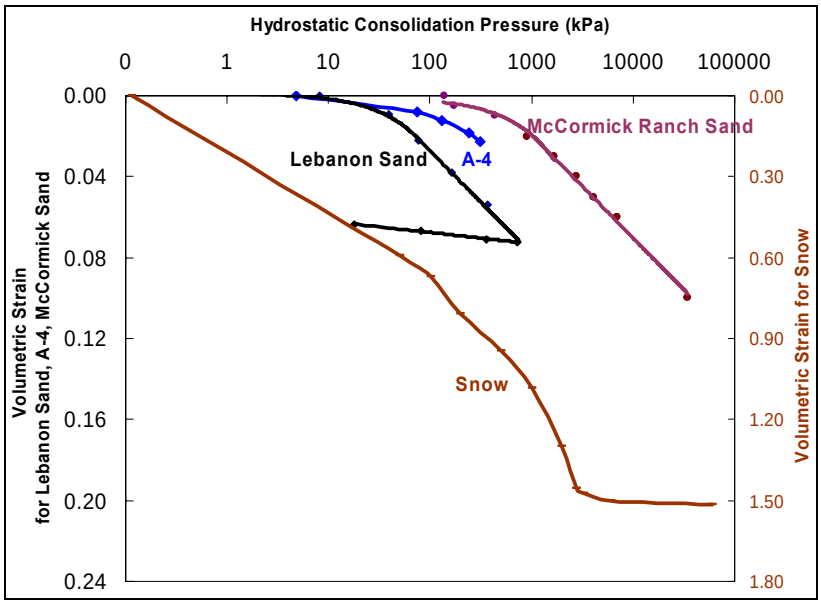

Figure 26. Pressure–volume relationship of Lebanon Sand compared with some other granular materials.

Figure 27 compares the shear failure lines for the thawing Lebanon Sand at three test conditions, the A4 silt, and snow. The shear lines are surprisingly different for the McCormick Sand (not shown in Fig. 27), which plots far above the other materials because of its large cohesion value. The slope, β, values cover a wide range also (14.6° to 55.8°), with the snow falling in the middle of the range at 22.4°.

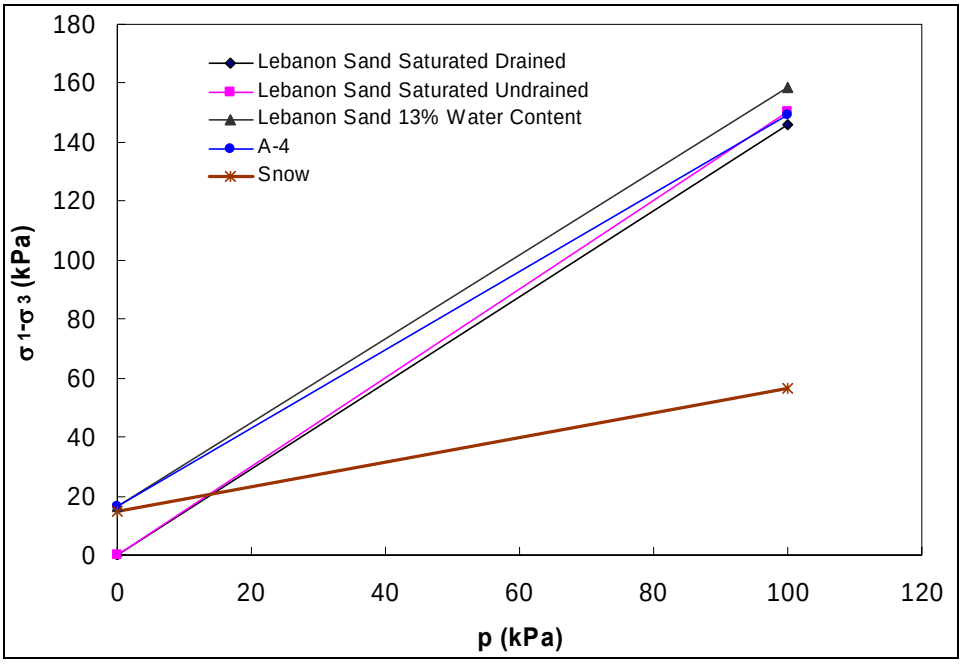

Figure 27. Drucker–Prager shear failure comparison of Lebanon Sand tested at different conditions, A-4 silt (saturated, drained), and snow.

7 SUMMARY AND CONCLUSIONS

Spring thaw creates unique conditions for soil. The thawing soil is often abnormally loose and wet as a result of the expansion from freezing and the subsequent excess meltwater being trapped in the thawing later by impermeable frozen layers below. The thaw layer is very weak, and it deforms plastically in both compaction and shear.

A frost-susceptible fine sand, Lebanon Sand, was subjected to a range of triaxial testing using density, moisture, and loading conditions similar to those experienced during the freeze–thaw testing in CRREL's Frost Effect Research Facility. A Capped Drucker–Prager (CDP) plasticity model was used to simulate the thawed soil using the commercial finite element code ABAQUS. Simulations of the triaxial tests were compared to the laboratory data. The material model was then implemented in three-dimensional finite element simulations to check model robustness and to validate it using direct shear test data, experiments on vehicle mobility on thawing soil, and a layered pavement system subjected to freeze–thaw.

The following summarize significant results of this study:

- A constitutive model of thawing soil was generated based on triaxial and hydrostatic test data.
- The model was implemented in several 3D finite models using the commercial finite element code ABAQUS.
- A small apparent cohesion is needed in the material model to obtain realistic behavior in the unconfined 3D model structural model of the wheel rolling on thawing ground.
- The 3D simulations attested to the robustness of the material model through the attainment of realistic model results under a variety of conditions.

REFERENCES

Arnold, G.K., A.R. Dawson, D.A.B. Hughes, and D. Robinson (2002) The application of shakedown approach to granular pavement layers. *Proceedings of the 9th International Conference on Asphalt Pavements*, Copenhagen, Vol. 1, paper 6-5.

Burton, N., P. Sullivan, M. Evans, and S. Shoop (2003) Constitutive modeling for A4 silt. ERDC-CRREL LR 03-16, U.S. Army Engineer Research and Development Center, Cold Regions Research and Engineering Laboratory, Hanover, New Hampshire.

DiMaggio, F.L., and I.S. Sandler (1971) Material model for granular soils. *Journal of the Engineering Mechanics Division, ASCE*, **97** (EM3): 935–950.

DiMaggio, F.L., and I.S. Sandler (1976) Generalized cap model for geological materials. *Journal of the Geotechnical Engineering Division, ASCE*, **102** (GT7): 683–699.

Haehnel, R., and S. Shoop (in prep.). Finite element modeling of thawing soil.

HKS (Hibbitt, Karlsson and Sorensen, Inc.) (1996) Analysis of geotechnical problems with ABAQUS. ABAQUS Course Notes, Pawtucket, Rhode Island.

HKS (Hibbitt, Karlsson and Sorensen, Inc.) (2002) ABAQUS theory manual. Pawtucket, Rhode Island.

Schofield, A.N., and C.P. Wroth (1968) *Critical State Soil Mechanics*. London, England: McGraw-Hill, Inc.

Scott, R.F. (1985) Plasticity and constitutive relations in soil mechanics. *Journal of Geotechnical Engineering*, **11** (5): 563–605.

Shoop, S.A. (1988) Research plan and experimental design for the study of vehicle mobility in thawing soils. Internal Report 1001, U.S. Army Cold Regions Research and Engineering Laboratory, Hanover, New Hampshire.

Shoop, S.A. (1990) Mechanisms controlling vehicle mobility on a thawing soil. *Proceedings of the 10th International Conference of the International Society of Terrain Vehicle Systems,* Kobe, Vol. I, p. 301–312.

Shoop, S.A. (1993) Thawing soil strength measurements for predicting vehicle performance. *Journal of Terramechanics*, **30** (6): 405–418.

Shoop, S.A. (2001) Finite element modeling of tire–terrain interaction. Ph.D. Dissertation, University of Michigan. Also ERDC-CRREL TR-01-38, U.S. Army Engineer Research and Development Center, Cold Regions Research and Engineering Laboratory, Hanover, New Hampshire.

Shoop, S.A., and K.S. Henry (1991) The effect of a geotextile on water migration and frost heave in a large scale test basin. *Transportation Research Record*, **1307**: 309–318.

Shoop, S.A., and S.R. Bigl (1997) Moisture migration during freeze and thaw of unsaturated soils: Modeling and large scale experiments. *Cold Regions Science and Technology*, **25**: 33–45.

Shoop, S.A., R. Haehnel, K. Kestler, K. Stebbings, and R. Alger (1999) Finite element analysis of a wheel rolling in snow. *Proceedings of the 10th International Conference on Cold Regions Engineering*, Lincoln, New Hampshire, p. 519–530.

Shoop, S.A., R. Haehnel, V. Janoo, and D. Harjes (2002) Seasonal deterioration of unsurfaced roads. *Proceedings, ASCE Cold Regions Engineering Conference*, Anchorage, Alaska, p. 311–322.

Shoop, S.A., R. Affleck, V. Janoo, and R. Haehnel (2003) Modeling deformation of thawing soil under vehicle loading. *Proceedings of the 3rd International Symposium on Deformation Characteristics of Geomaterials*, Lyon, France, p. 931–938.

U.S. Army Corps of Engineers (COE) (1970) Engineering and design, Laboratory soils testing. Appendix X, Triaxial compression tests. Engineer Manual EM 1110-2-1906.

Wood, D.M. (1990) *Soil Behavior and Critical State Soil Mechanics*. New York: Cambridge University Press.

APPENDIX A. GEOTECHNICAL CHARACTERIZATION DATA SUMMARY FOR LEBANON SAND

A controlled full-scale freeze–thaw test using Lebanon Sand was conducted in the test basin of the Frost Effects Research Facility (FERF). The test area was 36.6 × 13.1 m and consisted of a 1.1-m layer of Lebanon Sand and a base layer of fill separated by a geotextile. The soil was compacted to the desired density and at a specified moisture content. Temperature and soil moisture sensors were installed. Several freeze–thaw cycles were created, and the moisture content in the soil was varied by changing the water table depth or by adding surface water to simulate rain or snowmelt. The soil is frozen from the surface downward using freezing panels and then thawed with an elevated, constant air temperature. When the frost reached the required depth, frost heave, temperature, and soil moisture were measured. Frozen cores were drilled during different freeze cycles to determine ice contents. Various strength tests were performed in the laboratory from frozen core specimens (Shoop 1990, 1993). When the soil thawed to the desired depth, moisture content, density, and in-situ strength were measured. In addition, mobility testing was conducted using the CRREL Instrument Vehicle (CIV) to determine traction and motion resistance under thawing conditions on half of the test area. Physical and hydraulic properties under frozen and unfrozen conditions were compiled (Shoop and Bigl 1997). The soil moisture characteristic was determined in the laboratory. Frost heave and water migration during freezing and thawing were characterized as well (Shoop and Henry 1991).

This appendix conatins the following sections:

A1. Strength of Frozen Samples

A2. Physical and Hydraulic Properties of Lebanon Sand

A3. Water Migration and Frost Heave Characteristics

A4. Shear Measurements

A5. Chemical Analysis.

A1. Strength of Frozen Samples

Strength tests were conducted from frozen cores taken from the FERF (Shoop 1988). Tests S-1, S-5, and S-6 were conducted at a frozen state with zero confining pressure, while tests S-2, S-3 and S-4 were conducted at room temperature with a 5-psi confining pressure. The strain rate for each test was maintained at approximately 10% strain per second, and radial strain was measured for the frozen samples only. Results for the stress–strain and Poisson's stress graphs are shown in Figures A.1.1 and A.1.2, respectively.

Table A1. Summary for strength tests of frozen samples.

Test samples	S-1	S-2	S-3	S-4	S-5	S-6
Peak force (lb)	3516	54	71	32	4691	2979
Peak stress (psi)	1117.9	16.8	17.8	8.1	1446.4	933.6
Strain at peak stress (%)	1.58	4.06	23.19	21.55	2.74	1.60
Displacement at peak stress (in.)	0.079	0.194	0.983	0.989	0.127	0.080
Secant modulus (kpsi)	70620	413.15	76.71	37.56	52780	58300
Temperature (°C)	–4				–4.4	–4.5
Average strain rate (%/s)	10.82	10.71	10.52	10.09	11.34	10.29
Poison's ratio at half peak stress	0.062				0.069	0.056
Poison's ratio at peak stress	0.202				0.214	0.282
Strain rate at peak stress (%/s)	10.02	10.36	11.21	10.84	10.71	9.31
Initial density (lb/ft^3)	117.87	116.59	114.40	107.42	117.72	113.81
Time to peak (ms)	158.0	392.0	2068.0	1988.0	256.0	172.0
Length of test (ms)	2002.0	2024.0	2120.0	2036.0	2016.0	2016.0
Sample weight (g)	479.19	461.48	451.95	452.17	458.32	472.78
Sample height (in.)	5.002	4.875	4.750	5.102	4.700	5.040
Sample diameter (in.)	1.986	1.985	2.009	2.001	2.005	2.000
Water content (%)	10.2	10.1	9.4	7.4	11.6	9.7
Test temperature (°C)	–6.0	22.0	22.0	22.0	–6.0	–6.0
Confining pressure (kPa)	0	5	5	5	0	0

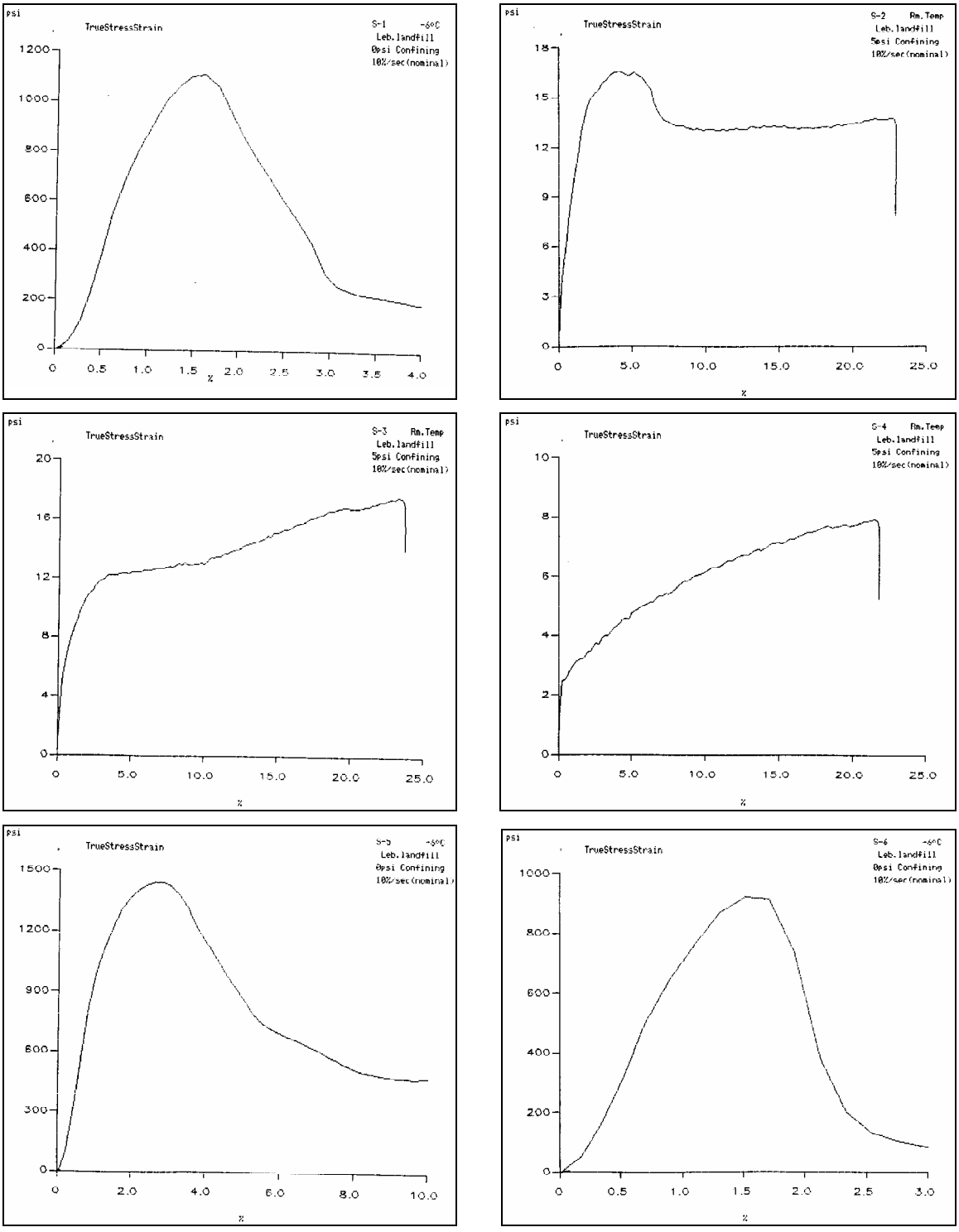

Figure A1. Stress–strain plots from the frozen cores.

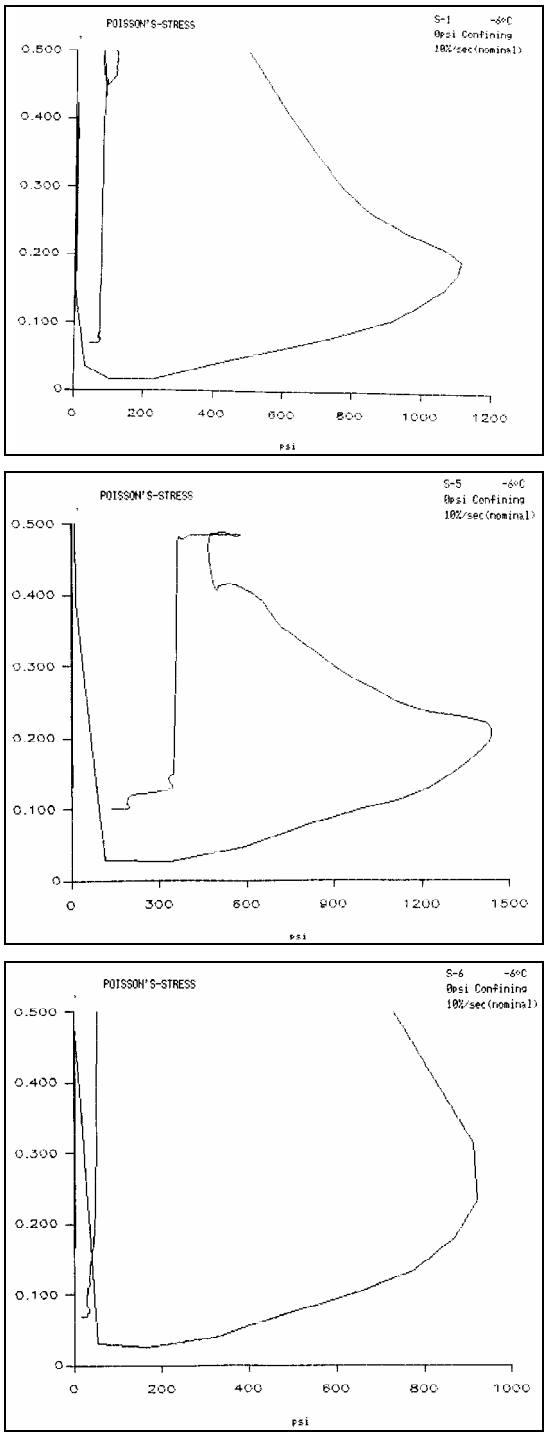

Figure A2. Poisson's ratio versus stress plots for S-1, S-5, and S-6 tests.

A2. Hydraulic Properties for Lebanon Sand

The soil moisture characteristics and hydraulic properties from the tests in the FERF are summarized below (Shoop and Bigl 1997).

Table A2. Physical and hydraulic properties of Lebanon Sand in the FERF test sections.

Properties		Layer 1 (0–15 cm)	Layer 2 (15–46 cm)	Layer 3 (46–107 cm)
Soil density (g/cm^3)		1.551*	1.678	1.697
Soil porosity (cm^3/cm^3)		0.419	0.419	0.419
Soil water characteristics:	Gardner's multiplier for moisture, A_w	1.962×10^{-5}	1.962×10^{-5}	1.962×10^{-5}
	Gardner's multiplier for moisture, α	1.975	1.975	1.975
Min. unfrozen water cont. (cm^3/cm^3)		0.03602	0.03602	0.03602
Saturated hydraulic conductivity (cm/hr)		1.6	1.6	1.6
Permeability characteristics:	Gardner's multiplier for hydraulic cond., A_K	1.590×10^{-9}	1.590×10^{-9}	1.590×10^{-9}
	Gardner's multiplier for hydraulic cond., β	4.623	4.623	4.623

*1.551 g/cm^3 for dry case, 1.620 g/cm^3 for wet case.

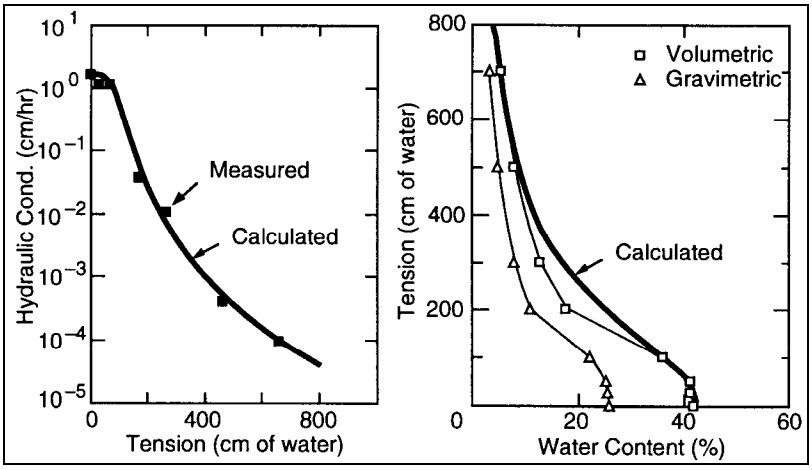

Figure A3. Hydraulic conductivity and moisture retention for Lebanon Sand.

Table A3. Warming data from an unfrozen water content test. Four samples tested with thawed gravimetric water contents are shown.

Temp (°C)	*Unfrozen water content (%), gravimetric*			
>0	5.52	10.87	15.74	20.65
–3.00	0.32		0.2	0.18
–1.93	0.63	0.41	0.39	0.37
–1.46	0.95	0.62	0.59	0.55
–0.96	1.26	0.82	0.79	0.74
–0.78	1.26	1.03	0.99	0.74
–0.59	1.58	1.03	0.99	0.92
–0.48	1.89	1.24	1.18	1.29
–0.37	1.89	1.65	1.38	1.29
–0.29	2.2	1.65	1.58	1.29
–0.17	2.52	2.06	1.78	1.67
–0.08	4.09	2.89	2.57	2.04
–0.04	4.72	3.51	2.96	2.59
–0.01		7.64	6.32	5.93

Table A4. Coefficients for modeling unfrozen water content.

Sample water content (%)	*Coefficients*	
	α	β
5.52	1.0045	–0.5629
10.87	0.7949	–0.5069
15.74	0.6685	–0.5297
20.65	0.6075	–0.5235

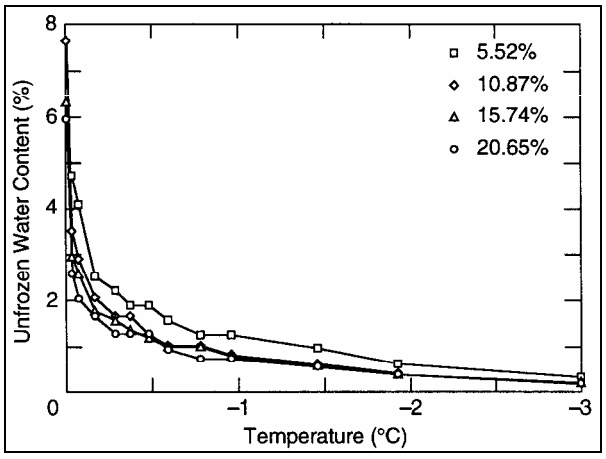

Figure A4. Warming data from unfrozen water content test on four samples tested with thawed gravimetric water contents.

A3. Water Migration and Frost Heave Characteristics

Results from the laboratory frost heave and moisture tension tests are shown in Figures A5 and A6, respectively (Shoop and Henry 1991).

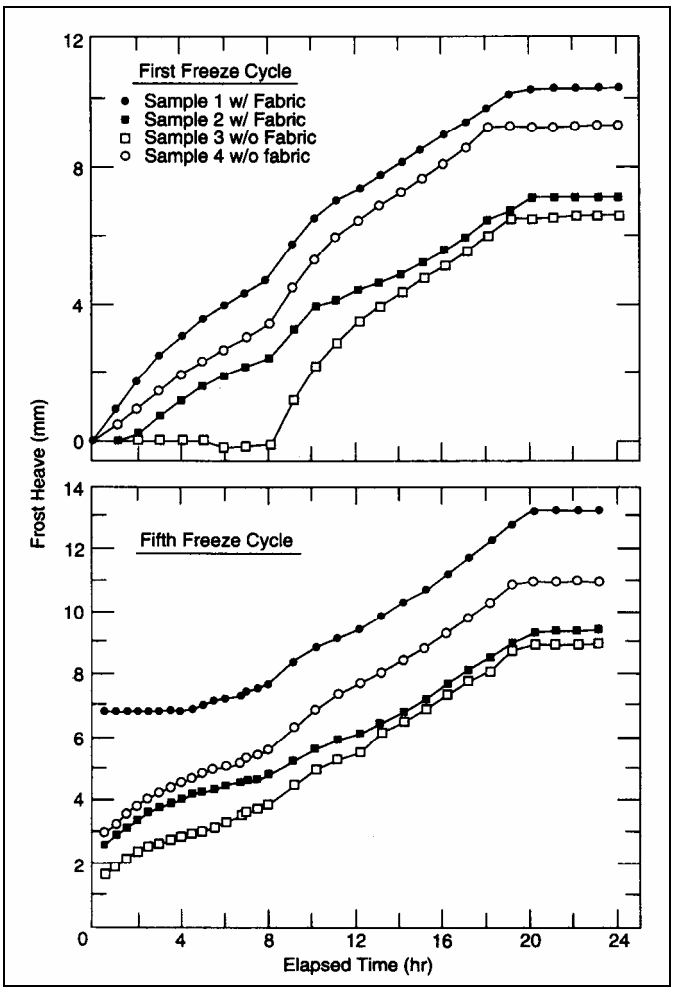

Figure A5. Laboratory frost heave test data.

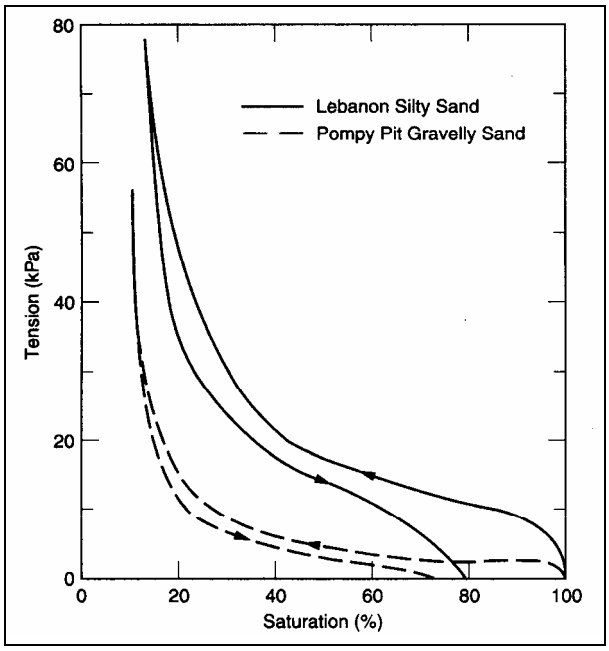

Figure A6. Laboratory moisture tension test.

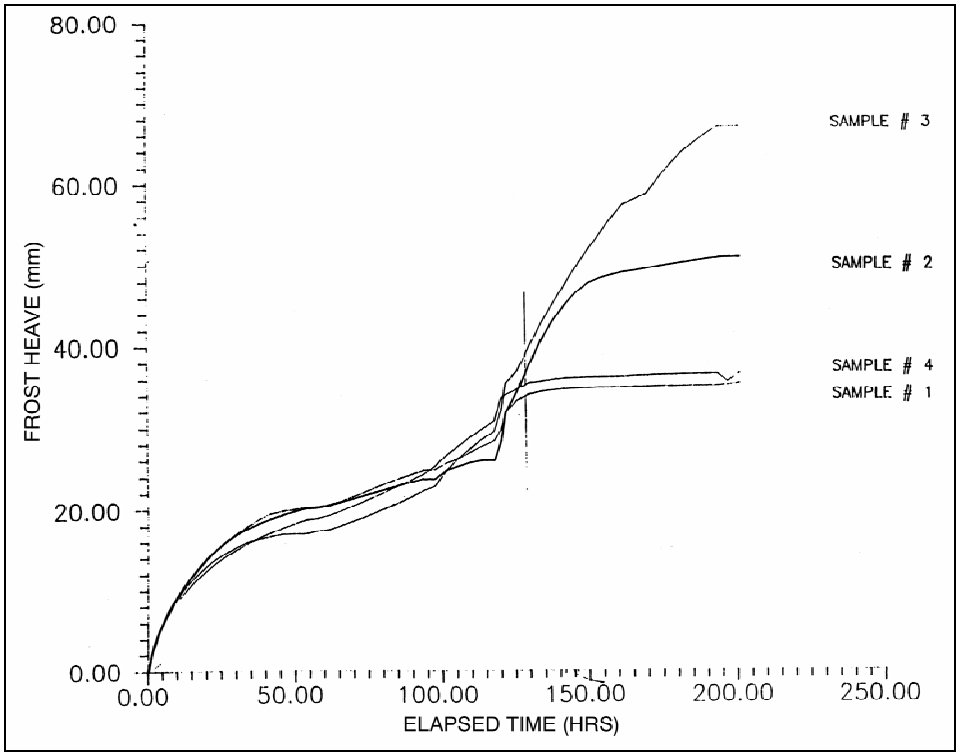

Figure A7. Frost heave test results.

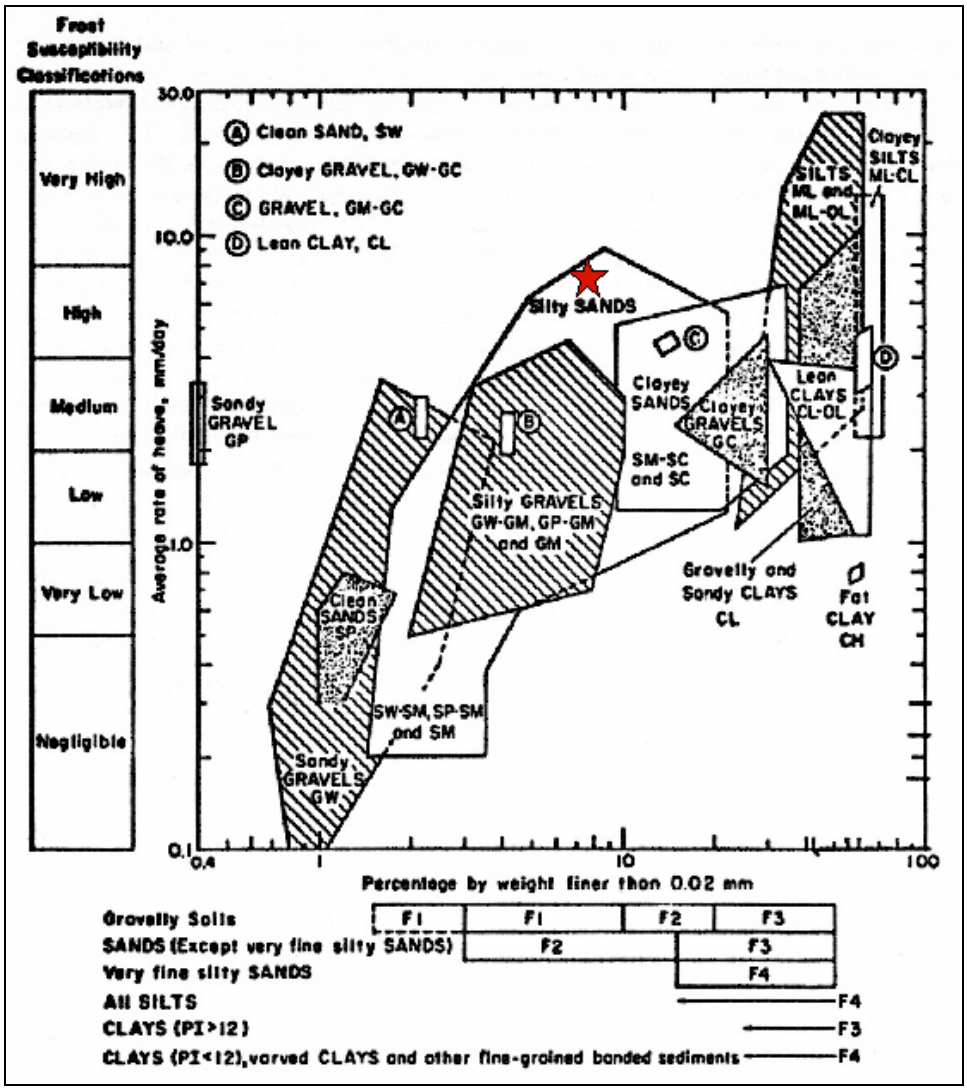

Figure A8. Lebanon Sand (red star) position on frost-susceptibility chart.

A4. Shear Measurements

The standard laboratory tests, including triaxial compression and direct shear, were performed along with in-situ tests using a shear annulus and CIV (Shoop 1990, 1993). Table A5 shows the summary from the triaxial compression test. The specimens used for the triaxial compression test were all machined from the various frozen cores taken from the FERF test section. The frozen samples were prepared for testing, then allowed to thaw overnight, and tests were performed at room temperature. Table A6 summarizes the direct shear test that was performed from some samples that were taken from the FERF test section as it thawed and from other samples that were prepared from the frozen cores similar to the triaxial test sample preparation. The shear annulus test was conducted in the FERF test section immediately prior to the mobility tests with the CIV and is listed in Table A7. From the mobility tests using the CIV, the maximum shear and normal stresses were developed from the tire–soil interface. The maximum shear stress applied to the soil was derived from the peak gross tractive force divided by the contact area of the tire. The normal stress was measured by dividing the normal load on the tire by the tire contact area. The maximum shear and normal stresses express in c' and ϕ' for various soil conditions are listed in Table A8. The loading comparison for each test method are listed in Table A9 and graphed in Figure A9. The effect of moisture content on ϕ' measured using the direct shear, shear annulus, and CIV methods showed that ϕ' increased until the soil liquid limit was met and then rapidly dropped (Figure A10). The calculated ϕ' from the CIV test with thaw depth is also shown in Figure A11.

Table A5. Triaxial test data (thawed cores).

Sample no.	*Confining pressure (kPa)*	*Failure stress (kPa)*	*Water content (%)*	*Dry density (g/cm^3)*	*Total density (g/cm^3)*
s-9	0	70.97	16.0	1.592	1.846
s-6	0	163.98	16.5	1.672	1.948
s-1	0	175.01	18.7	1.654	1.963
s-3	0	207.39	18.8	1.659	1.971
s-4	34.4	55.81	11.6	1.539	1.718
s-3	34.4	122.64	7.4	1.704	1.830
s-2	34.4	115.75	9.7	1.701	1.866
s-5	68.9	228.75	21.7	1.558	1.897
s-12	68.9	289.38	18.4	1.630	1.931
s-7	137.8	319.70	15.1	1.574	1.811
s-11	137.8	266.64	12.5	1.629	1.833
s-4	137.8	320.39	18.6	1.650	1.957

Table A6. Direct shear test data.

Sample no.	Normal load (N)	Peak load (N)	Residual load (N)	Area (cm^2)	Water content (%)	Dry density (g/cm^3)	Total density (g/cm^3)
12	243.48	146.78	93.41	30.53	21.5	1.501	1.823
8	243.48	179.25	160.13	30.61	12.6	1.573	1.772
tc12r	243.48	224.18	164.58	31.41	12.5	1.696	1.909
tc12	243.48	231.30	157.90	31.41	12.3	1.696	1.905
tc11	243.48	232.63	151.23	31.41	12.6	1.696	1.910
2	243.48	236.19	179.25	30.64	10.6	1.702	1.883
7	360.29	293.57	265.10	30.51	12.4	1.675	1.882
tc12	360.29	320.26	271.33	31.41	11.6	1.696	1.894
5	360.29	324.70	240.19	30.66	18.1	1.695	2.002
tc11	360.29	326.04	233.52	31.41	12.5	1.696	1.909
tc12r	360.29	346.94	263.32	31.41	12.3	1.696	1.905
4	360.29	373.63	272.22	30.35	16.9	1.735	2.028
6	556.00	389.20	345.61	30.75	20.5	1.470	1.772
11	556.00	411.44	350.06	30.51	10.6	1.631	1.804
9	556.00	422.56	341.16	30.53	19.1	1.614	1.922
tc12r	556.00	428.34	311.36	31.41	13.5	1.696	1.925
tc12	556.00	437.02	311.36	31.41	11.9	1.696	1.898
tc11	556.00	444.80	400.32	31.41	12.6	1.696	1.911
10	711.68	494.84	422.56	30.41	21.6	1.451	1.765
tc12	711.68	533.76	355.84	31.41	15.8	1.696	1.964
13	711.68	550.44	442.58	30.25	19.7	1.627	1.947
tc12r	711.68	551.55	389.20	31.41	11.5	1.696	1.892
tc12r	711.68	578.24	378.08	31.41	12.7	1.696	1.911
1	711.68	633.84	456.81	30.57	17.0	1.719	2.011

Table A7. Shear annulus test data.

Date	c (kPa)	ϕ (degrees)	Thaw depth (cm)	Water content (%)	Dry density (g/cm^3)	Total density (g/cm^3)	Saturation (%)
Nov 9	4.44	33.5	3.81	20.0	1.509	1.811	67.9
Nov 10	0.88	36.5	10.16	23.4	1.546	1.907	83.9
Nov 10	0.30	37.9	10.16	23.4	1.546	1.907	83.9
Nov 10	0.92	36.6	10.16	23.4	1.546	1.907	83.9
Dec 20	0.90	38.4	*	13.0	1.699	1.920	58.9
Dec 20	1.54	37.9	*	13.0	1.699	1.920	58.9
Dec 27	2.82	36.8	*	9.0	1.611	1.756	35.6
Dec 27	4.13	34.8	*	9.0	1.611	1.756	35.6
Dec 27	3.17	33.5	*	9.0	1.611	1.756	35.6
Dec 28	2.27	33.1	3.81	24.2	1.516	1.883	82.9
Dec 30	3.72	29.9	5.08	27.0	1.547	1.965	97.0
Dec 30	0.25	30.7	5.08	27.0	1.547	1.965	97.0

* Soil totally thawed.

Table A8. *c′* and ϕ′ calculated from CIV tests for each soil condition.

Date	c′ (kPa)	ϕ′ (degrees)	Thaw depth (cm)	Water content (%)	Dry density (g/cm^3)	Total density (g/cm^3)	Saturation (%)
Nov 9	16.39	28.0	3.81	20.0	1.5088	1.811	67.9
Nov 10	15.36	20.0	10.16	23.4	1.5456	1.907	83.9
Dec 20	37.34	21.6	60.96	13.0	1.6992	1.920	58.9
Dec 27	46.64	17.0	60.96	9.0	1.6112	1.757	35.6
Dec 28	12.88	23.3	3.81	24.2	1.5152	1.883	83.0
Dec 30	40.37	11.0	8.89	27.0	1.5472	1.965	97.0

Table A9. Loading comparison for each test method.

	Normal stress (kPa)	Deformation rate (cm/s)	Area of applied normal load (cm^2)
Triaxial	34–227	1.27	20.6
Direct shear	80–234	0.08	31.6
Shear annulus	5–36	4.2	126
Instrumented vehicle wheel	124–200	10–40	387–581

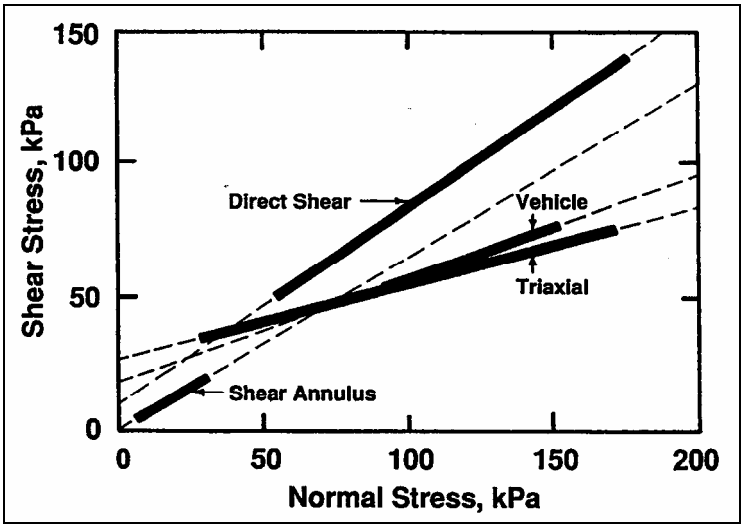

Figure A9. Comparison of failure envelopes for each test method. Solid lines mark the range of normal stress for each test.

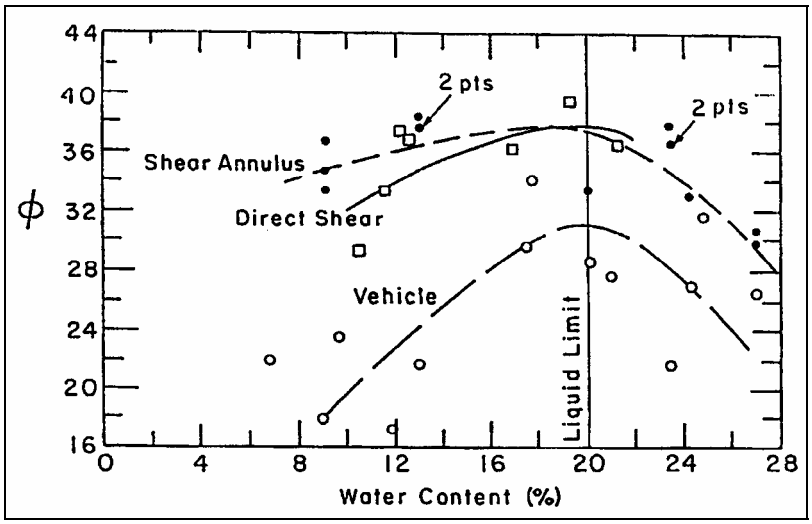

Figure A10. Calculated ϕ′ with water content.

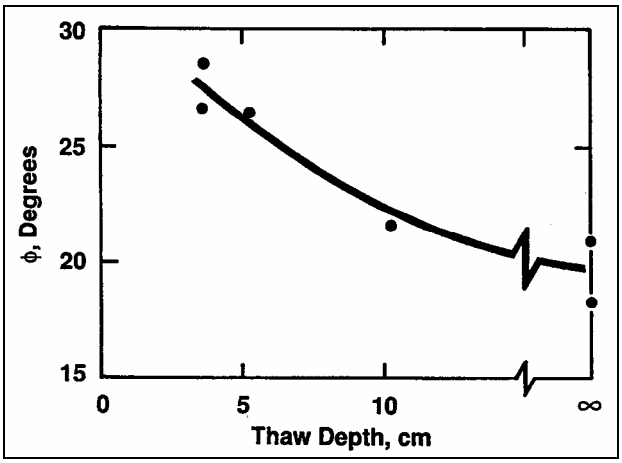

Figure A11. Calculated ϕ′ from the CIV test with thaw depth.

Table A10. Direct shear data for Lebanon Sand at constant density of 106 pcf (cross section area = 4.831 in^2; volume = 0.007 ft^3), September 1990.

Sample no.	Normal load (lb)	W (%)	Peak shear load (lb)	Mean peak (lb)
1	4.8	8.0	9.0	10.9
2			11.0	
3			12.5	
4			11.0	
5			10.1	
6			11.6	
1A	25.3	8.0	29.0	27.8
2A			24.0	
3A			25.5	
4A			30.0	
5A			26.5	
6A			32.4	
1	4.8	12.0	11.9	11.0
2			10.8	
3			11.0	
4			10.3	
1A	25.3	12.0	31.6	30.7
2A			32.4	
3A			28.1	
1	4.8	17.0	13.6	13.5
2			15.0	
3			12.0	
1A	25.3	17.0	31.0	31.8
2A			32.0	
3A			32.5	
1	4.8	21.0	10.0	9.9
2			10.0	
3			9.6	
1A	25.3	21.0	22.0	22.5
2A			22.5	
3A			23.0	
1	4.8	25.0	6.0	6.0
2			6.0	
3			6.1	
1A	25.3	25.0	18.7	18.7
2A			19.3	
3A			18.0	
1	54.7	Liquid	44.5	
2			42.8	
3			47.0	
4	81.0	Liquid	67.0	
5			65.0	
6			69.0	
7	125.0	Liquid	86.2	
8			80.9	
9			84.6	
10	160.0	Liquid	113.9	
11			118.4	
12			115.8	

A5. Chemical Analysis

Table A10. Chemical analysis for Lebanon Sand, 5 Jan 1997.

P	152 Mg/kg
Na	0
K	10
Ca	909
Mg	1000+
pH	6.6
OM	0.32 %

APPENDIX B. SOIL CONDITIONS FOR SATURATED TRIAXIAL SHEAR AND HYDROSTATIC TESTS

The specimens for the saturated triaxial tests were prepared based on the procedures outlined in Appendix X, EM (Engineer Manual) 1110-2-1906 (U.S. Army COE 1970). These specimens were molded at specific moisture contents and densities for the drained and undrained tests. The specimens were then back-pressure saturated, and after-saturation conditions were also determined for each sample. Tables B1 and B2 are summaries of the moisture content and dry densities for each samples before and after saturation conditions for both drained and undrained triaxial tests. The conditions for the hydrostatic consolation test are shown in Table B3. The pore pressure and displacement measurements were recorded for the saturated undrained triaxial test (Fig. B1).

Table B1. Lebanon Sand drained shear tests.

Test no.		Water content (%)	Dry density (pcf)	Void ratio
2DS1	Initial Condition	9	108.8	0.53
	After Saturation	18	108.9	0.53
2DS2	Initial Condition	9	108.7	0.53
	After Saturation	18	108.7	0.53
4DS2	Initial Condition	9	108.7	0.53
	After Saturation	18	108.7	0.53
6DS1	Initial Condition	9	108.2	0.54
	After Saturation	18	110.0	0.52
6DS2	Initial Condition	9	108.3	0.54
	After Saturation	18	108.5	0.54

Table B2. Lebanon Sand undrained shear tests.

Test no.		Water content (%)	Dry density (pcf)	Void ratio
2US1	Initial Condition	13	109.4	0.52
	After Saturation	17	109.6	0.52
2US3	Initial Condition	13	109.1	0.53
	After Saturation	20	110.0	0.52
4US1	Initial Condition	13	114.0	0.46
	After Saturation	18	115.0	0.45
4US2	Initial Condition	9	108.0	0.54
	After Saturation	20	110.6	0.51
4US3	Initial Condition	9	107.9	0.54
	After Saturation	20	109.2	0.53
6US2	Initial Condition	9	107.8	0.55
	After Saturation	20	109.3	0.53
6US3	Initial Condition	9	108.9	0.53
	After Saturation	20	111.3	0.50

Table B3. Lebanon Sand hydrostatic consolation test.

Type of test	Hydro stress (psi)	Hydro stress (kPa)	Vol. strain (%)	Vol. strain	Coeff. perm. (cm/s)	Void ratio, e
Load (LK3)	1.2	8.2	0	0.000	2.7×10^{-4}	0.52
Load (LK6)	5.6	38.9	0.89	0.009	2.0×10^{-4}	0.51
Load (LK12)	11.0	76.0	2.20	0.022	1.4×10^{-4}	0.49
Load (LK25)	23.8	163.9	3.82	0.038	8.9×10^{-5}	0.47
Load (LK50)	53.0	365.5	5.39	0.054	8.0×10^{-5}	0.45
Load (LK10)	104.4	720.1	7.21	0.072	7.2×10^{-5}	0.42
Rebound (RK50)	51.8	356.9	7.12	0.071	8.6×10^{-5}	0.42
Rebound (RK12)	11.9	82.2	6.66	0.067	8.9×10^{-5}	0.43
Rebound (RK3)	2.6	17.8	6.36	0.064	7.7×10^{-5}	0.43

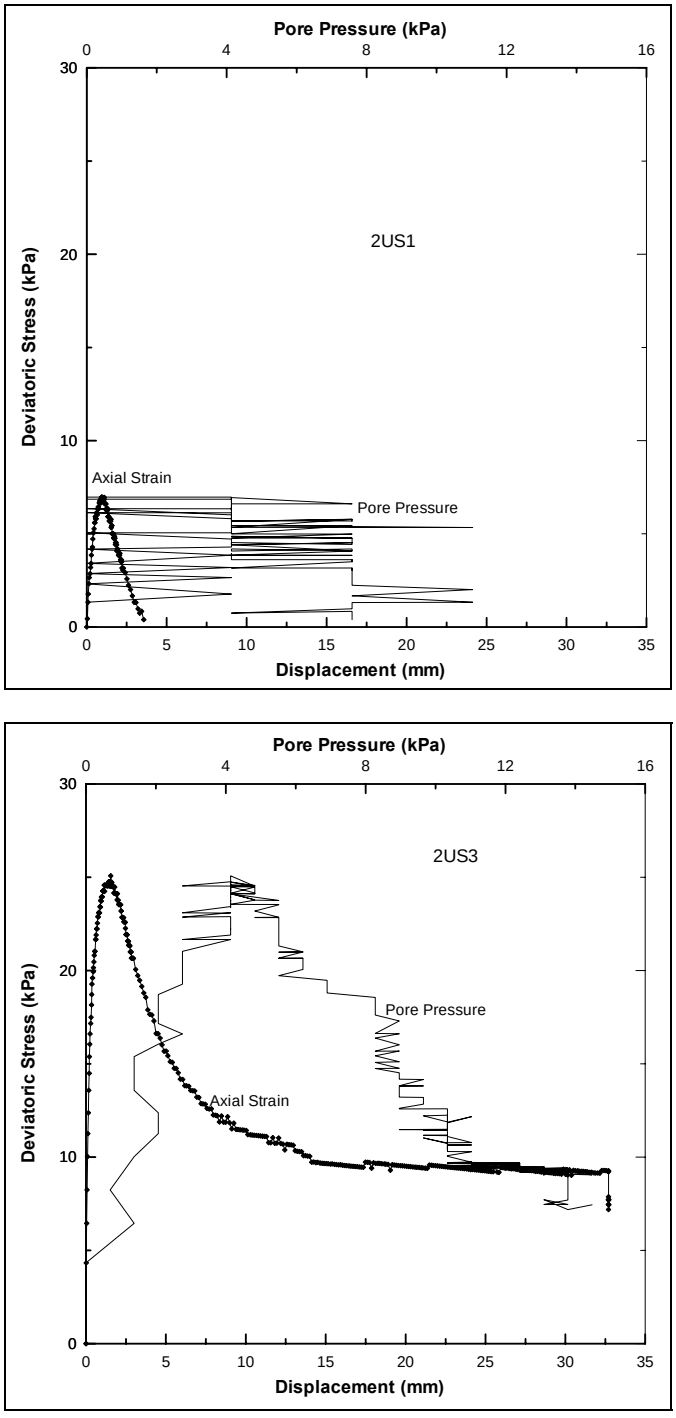

Figure B1. Deviatoric stress versus displacement and pore water pressures for the saturated undrained triaxial tests.

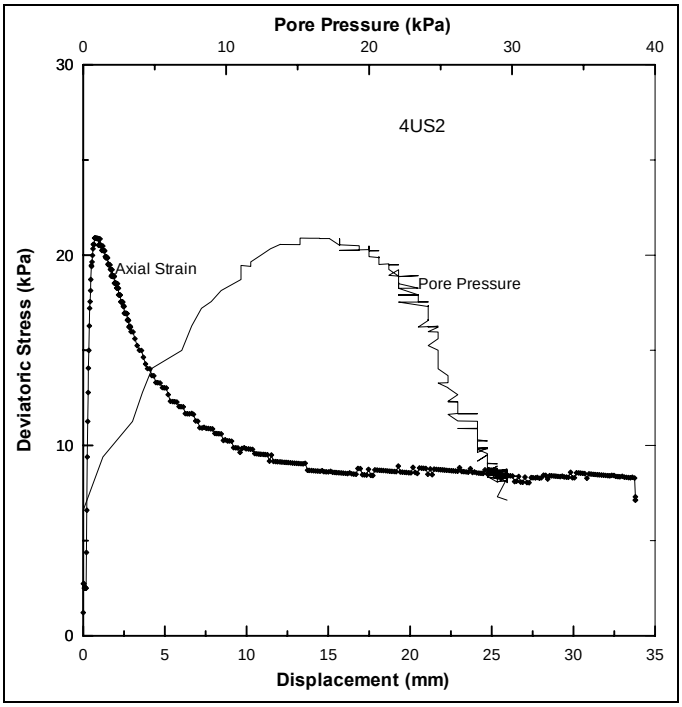

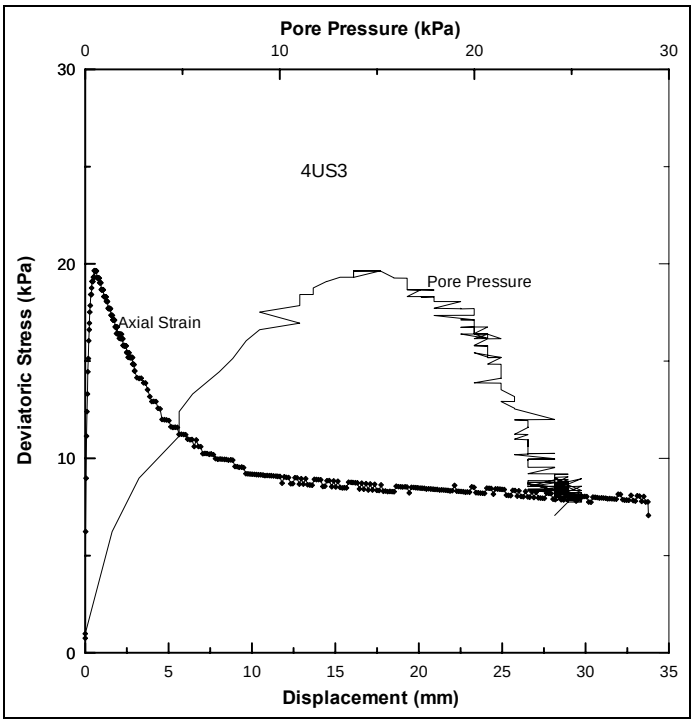

Figure B1 (cont.).

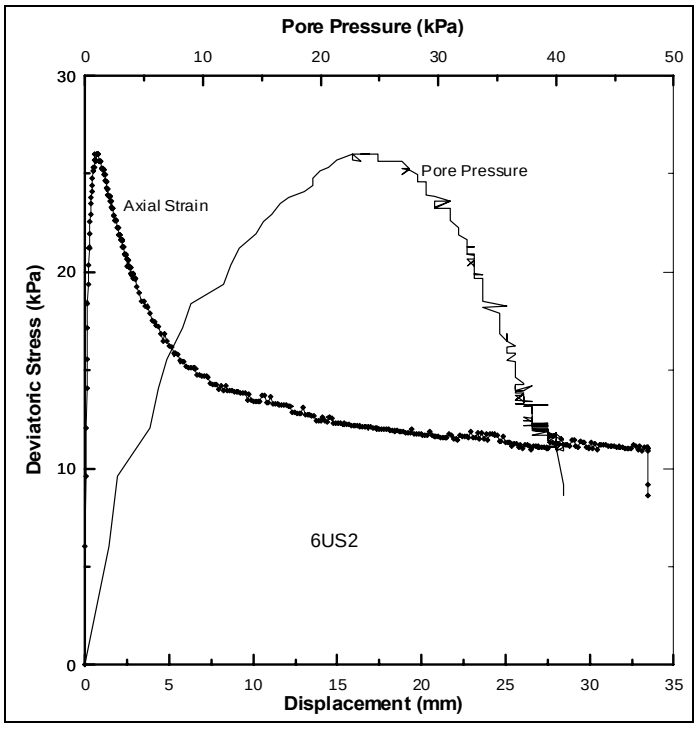

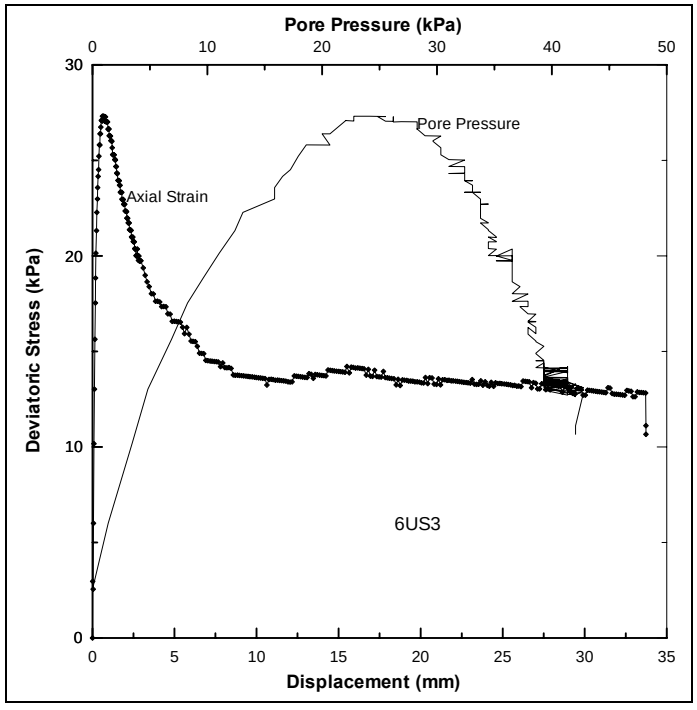

Figure B1 (cont.).

APPENDIX C. DATA FOR UNSATURATED TESTS PERFORMED AT OPTIMUM MOISTURE CONTENT AND DENSITY

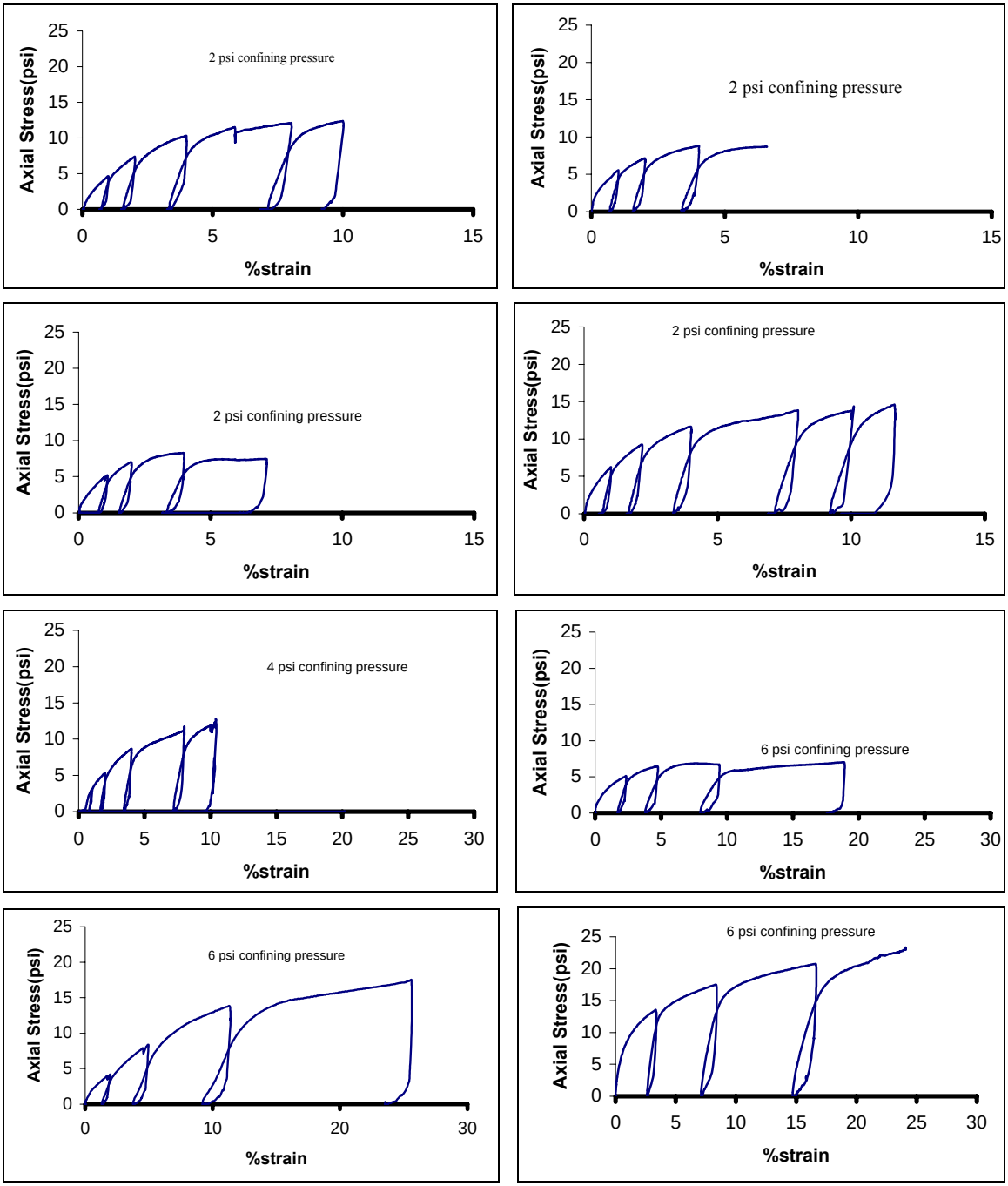

Figure C1. Unsaturated triaxial tests (undrained).

Table C1. Summary of Lebanon Sand undrained shear tests for samples at 13% moisture content.

Test no.	Average σ_3 (confining pressure) (kPa)	Peak q ($\sigma_1 - \sigma_3$) (kPa)	Max. mean stress, *p* (kPa)
2.1	14	57	33
2.3	14	61	34
2.4	14	86	43
2.5	14	101	47
4.2	27	83	55
6.1	41	159	94
6.2	42	121	82

Table C2. Young's Modulus calculations

Test name	2.4	2.3	2.1	2.5	4.2	6.3	6.2	6.1
Confining pressure, psi	2	2	2	2	4	6	6	6
Values per load, psi	2766.7	1940.0	1660.0	2200.0	1780.0	900.0	583.3	1727.3
	1287.5	1355.5	1080.0	1411.1	1240.0	541.7	214.3	1300
	1250.0	1111.1	1150.0	1125.0	1277.8	295.0	933.3	750
	1111.1			1111.1	1000.0			
				1375.0				
Average	1603.8	1468.8	1296.7	1444.4	1324.5	578.9	576.9	1259.1
Average	1453.4				1324.5	805.0		
Total avg.	1231.3 psi (8489.5 kPa)							

APPENDIX D. ABAQUS CODE FOR TRIAXIAL TEST SIMULATION

```
** Simulation of triaxial tests on Lebanon Sand
Material
**
** Sample size, 2.8" DIA x 5.5" High
**
*HEADING
Lebanon Sand, Triaxial test
******************************************************
** Soil Node and Element Definition
**
*PARAMETER
disp=1.375 #inches
press=2 #psi
cohes=10000 #Pa
beta=55.8 #degrees
ecc=0.45
e_o=0
youngs=8.5e6 #Pa
v=0.36
press=press*6895 #Pa
disp=disp/2*.0254 #m
******************************************************
*NODE, NSET=CYL
 1, 0., 0.
 2, 0.0356, 0.
 3, 0., -0.1397
 4, 0.0356, -0.1397
**
*ELEMENT, TYPE=CAX4, ELSET=CYLINDER
 1, 1, 3, 4, 2
******************************************************
**
** Soil Material Definition
**
*SOLID SECTION, ELSET=CYLINDER, MATERIAL=dpsoil
*MATERIAL, NAME=BAS_EL
*DENSITY
1890.
```

```
*ELASTIC
<youngs>,<v>
**
*MATERIAL,NAME=dpsoil
*ELASTIC
<youngs>,<v>
*CAP PLASTICITY
** COHESN, BETA, BIGR, EVOLPI, ALPHA, BIGK
<cohes>,<beta>,<ecc>,<e_o>,,1.
*CAP HARDENING
** PB is hydrostatic stress in pascals, EVOLP is vol.
strain and unitless**
 8.2e3,0.
 38.9e3,.009
 76.0e3,.022
163.9e3,.038
365.5e3,.054
720.1e3,.072
*DENSITY
1890.
******************************************************
** Boundary Conditions
**
*BOUNDARY, OP=NEW
 1, 1,, 0.
 3, 1,, 0.
 3, 2,, 0.
 4, 2,, 0.
**
*INITIAL CONDITIONS, TYPE=STRESS, GEOSTATIC
CYLINDER,-264.,-0.1397,0.,0.,1.,1.
******************************************************
** Step 1, Geostatic, LoadCase, Default
**
*STEP, INC=500, UNSYMM=YES
**, NLGEOM
Apply Hydrostatic Compression
*STATIC
 .5, 1.0, 1.E-8,
*DLOAD, OP=NEW
CYLINDER, P3, <press>
```

```
CYLINDER, P4, <press>
**
*OUTPUT, FIELD, FREQUENCY=1
*ELEMENT OUTPUT
S,E,PEQC
*NODE OUTPUT
U
*OUTPUT, HISTORY, FREQUENCY=1
*ELEMENT OUTPUT, ELSET=CYLINDER
S,E,PEQC
*NODE OUTPUT, NSET=CYL
U,RF
*END STEP
**********************************************************
** Load 1.375 inch displacement
**
*STEP, INC=10000, UNSYMM=YES
Load to 1.375 in displacement
**, NLGEOM
**STATIC, DIRECT
**0.01
*STATIC
0.01,1.0,.00000001
*BOUNDARY, OP=MOD
1, 2,, -<disp>
2, 2,, -<disp>
*END STEP
```

APPENDIX E. RESULTS FOR TRIAXIAL TEST SIMULATIONS

Initially, small cohesions such as 3000, 1200, and 1.0×10^{-5} were used with alternating beta values of 34.4 and 26.6º. The graphs plotted from these data showed that the results grossly underestimated the laboratory test data. The next logical step was to increase the cohesion while keeping the beta the same as in previous runs. Varying the cohesion between 15 and 40 kPa raised the simulated deviatoric stress to a level that was sufficient to fit the control data. However, the slope of the simulated data was very steep and then very flat with an abrupt maximum, while the slope of the laboratory data changed more gradually. To correct this, the eccentricity was changed from a standard of 0.45 in the previous runs to 0.1 and 0.3 (Fig. E1).

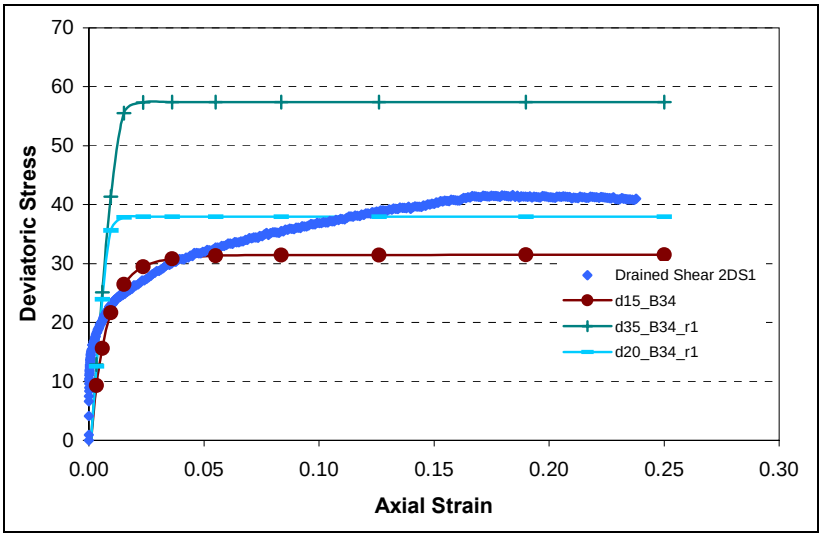

Figure E1. Comparison between results from simulation runs using higher cohesions (15, 20, and 35 kPa) with changed eccentricity (0.1) and laboratory data for 14 kPa (2 psi) confining pressure. The plots for the 28- and -40 kPa (4 and 6psi) confining pressures exhibited the same behavior as the 14-kPa plot.

The data plots showed that this was not the answer to the slope problem; if anything, this change made the graphs steeper than before. In two simulation tests the initial volumetric plastic strain was also changed to 0.007 from the standard 0.001, and again it made no difference in the plots (Fig. E2).

Finally the switch was made from a Young's modulus of 1.73e6 to 8.50e6 (the final value averaged in Table C2). In addition, a new beta value was recalculated (55.8º) based on the ABAQUS definition of deviator stress, *q*. The

eccentricity was also returned to its original 0.45, and the initial strain was set at 0. Six simulations were run using these values and a cohesion of 1.0×10^{-5}, and the resulting graphs fit almost perfectly with our control test data (Fig. E3).

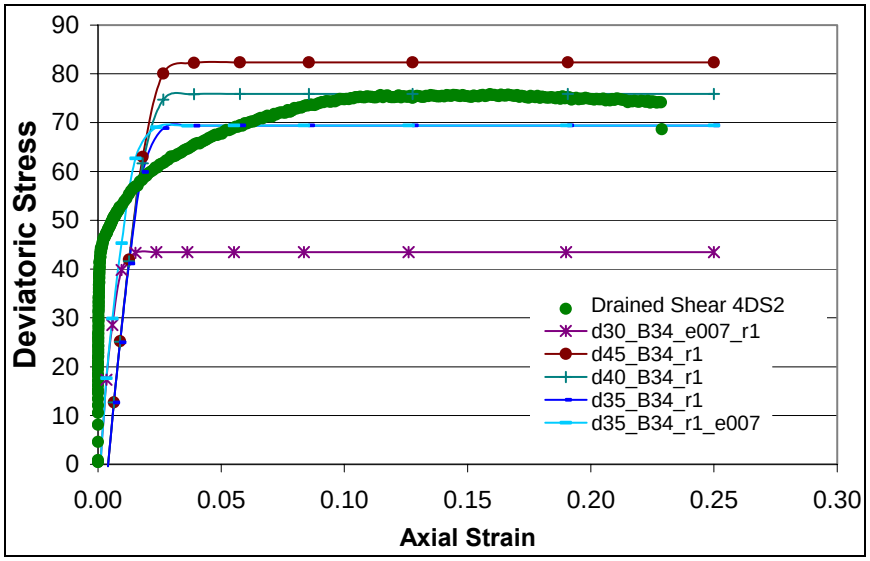

Figure E2. Comparison of changed initial volumetric plastic strain to laboratory data and unchanged volumetric plastic strains for 28 kPa (4 psi) confining pressure. There were no simulations performed for the change in initial volumetric plastic strain for 14 and 40 kPa (2 and 6 psi) confining pressures.

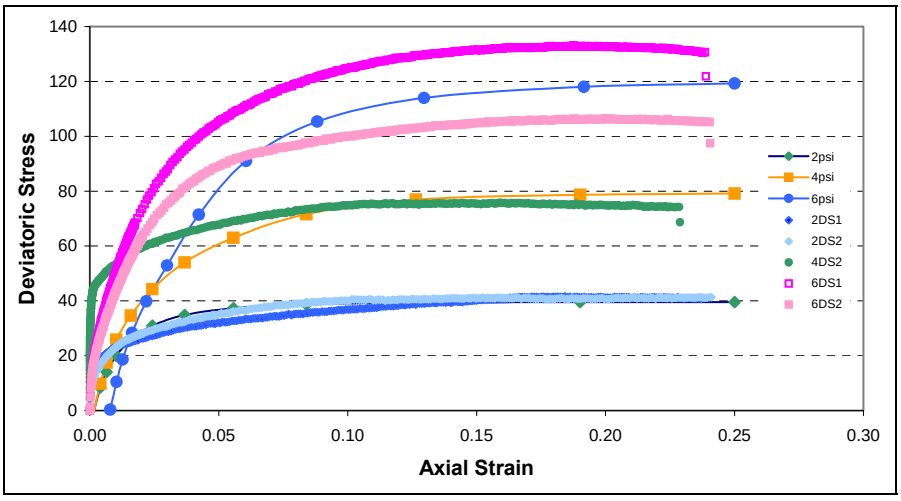

Figure E3. Comparison of new cohesion and beta graphs with laboratory data for 2, 4, and 6 psi confining pressure (d = 1.0×10^{-5}, beta = 55.8°, evol = 0, eccentricity = 0.45).

However, when this set of parameters was put into the 3-D simulation, the material model faltered and would not work correctly. The top layer of the soil expanded erroneously because there was insufficient material cohesion to support a tensile load (Fig. E4). The final adjustment was to increase the cohesion to values of 5 and 10 kPa (Fig. E5). While some sacrifice was made with the fit of the model to the laboratory data, the 3-D model ran smoothly and gave a satisfactory result. A final set of parameters was obtained that gave a reasonable fit to both lab and field observations.

The results of the finite element simulations of the triaxial tests are given in Table E1.

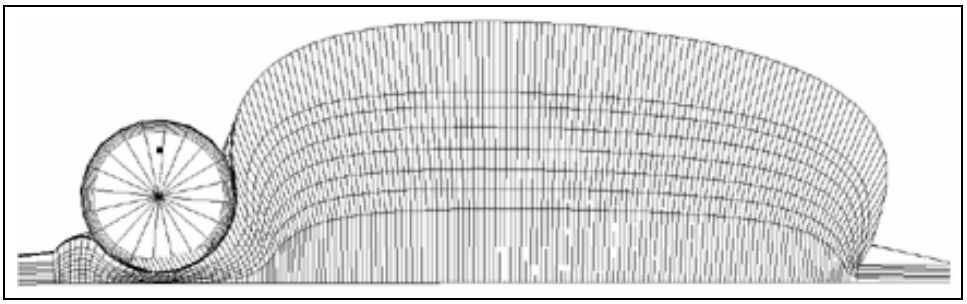

Figure E4. 3-D ABAQUS simulation of a tire in soft soil with large expansion caused by shearing of zero cohesion material (vertical exaggeration for illustration).

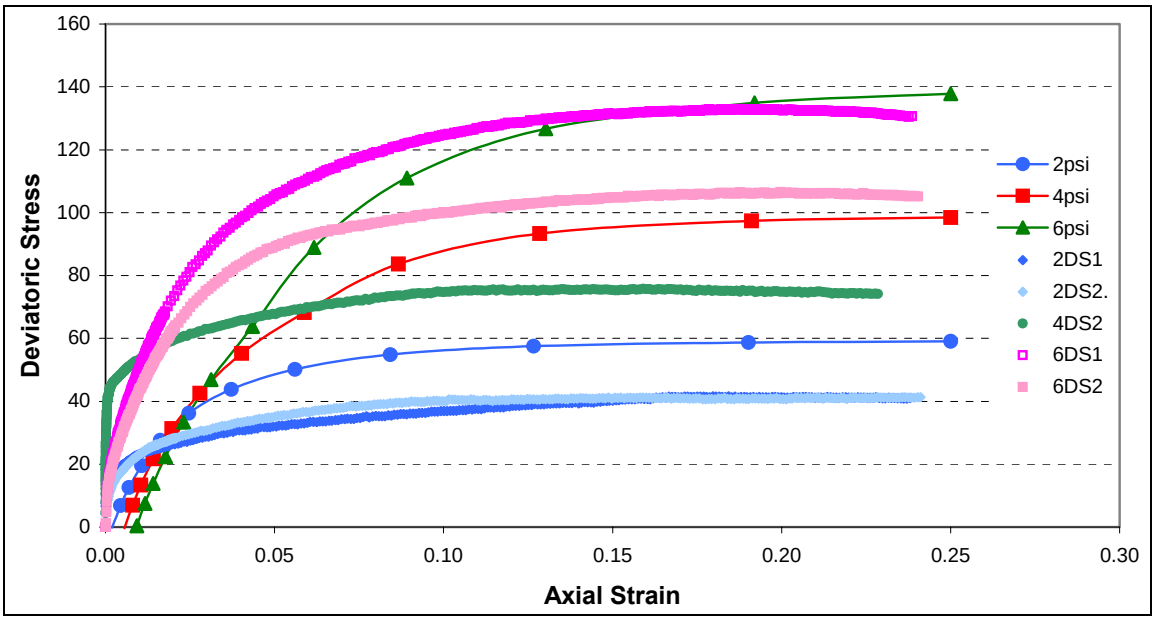

Figure E5. Comparison of final model parameters with laboratory data for 2, 4, and 6 psi confining pressure.

Table E1. Summary of triaxial test simulations and test results.

d (Pa)	Beta (º)	R	Confining press (psi)	Young's modulus	Volumetric plastic strain	Peak deviatoric stress (kPa)
3000	34.4	0.45	2	1.73×10^{6}	0.001	12
3000	26.6	0.45	2	1.73×10^{6}	0.001	7
1200	34.4	0.45	2	1.73×10^{6}	0.001	13
1200	26.6	0.45	2	1.73×10^{6}	0.001	9
1200	14.4	0.45	2	1.73×10^{6}	0.001	5
1200	55.8	0.45	2	1.73×10^{6}	0.001	40
1.00×10^{-5}	14.4	0.45	2	1.73×10^{6}	0.001	4
1.00×10^{-5}	34.4	0.45	2	1.73×10^{6}	0.001	12
1.00×10^{-5}	26.6	0.45	2	1.73×10^{6}	0.001	7
5000	55.8	0.45	2	1.73×10^{6}	0.001	47
1.00×10^{-5}	14.4	0.45	4	1.73×10^{6}	0.001	7
1.00×10^{-5}	26.6	0.45	4	1.73×10^{6}	0.001	15
1.00×10^{-5}	34.4	0.45	4	1.73×10^{6}	0.001	24
1200	34.4	0.45	4	1.73×10^{6}	0.001	25
3000	26.6	0.45	4	1.73×10^{6}	0.001	15
3000	34.4	0.45	4	1.73×10^{6}	0.001	24
15000	26.6	0.1	2	1.73×10^{6}	0.001	26
15000	26.6	0.3	2	1.73×10^{6}	0.001	26
15000	34.4	0.1	2	1.73×10^{6}	0.001	32
15000	34.4	0.3	2	1.73×10^{6}	0.001	32
15000	26.6	0.1	4	1.73×10^{6}	0.001	34
15000	26.6	0.3	4	1.73×10^{6}	0.001	34
15000	34.4	0.1	4	1.73×10^{6}	0.001	44
15000	34.4	0.3	4	1.73×10^{6}	0.001	44
40000	15	0.1	4	1.73×10^{6}	0.001	51
15000	26.6	0.1	6	1.73×10^{6}	0.001	42
15000	26.6	0.3	6	1.73×10^{6}	0.001	42
15000	34.4	0.1	6	1.73×10^{6}	0.001	55
15000	34.4	0.3	6	1.73×10^{6}	0.001	55
7540	34.4	0.45	2	1.73×10^{6}	0.001	22
7540	26.6	0.45	2	1.73×10^{6}	0.001	17
3040	34.4	0.45	2	1.73×10^{6}	0.001	16
3040	26.6	0.45	2	1.73×10^{6}	0.001	12
15000	34.4	0.45	2	1.73×10^{6}	0.001	32
35000	34.4	0.1	2	1.73×10^{6}	0.001	57

40000	34.4	0.1	2	1.73×10^{6}	0.001	64
20000	34.4	0.1	2	1.73×10^{6}	0.001	38
15000	34.4	0.45	4	1.73×10^{6}	0.001	44
7540	26.6	0.45	4	1.73×10^{6}	0.001	25
7540	34.4	0.45	4	1.73×10^{6}	0.001	34
30000	34.4	0.1	4	1.73×10^{6}	0.007	44
45000	34.4	0.1	4	1.73×10^{6}	0.001	82
40000	34.4	0.1	4	1.73×10^{6}	0.001	75
35000	34.4	0.1	4	1.73×10^{6}	0.001	69
35000	34.4	0.1	4	1.73×10^{6}	0.007	69
15000	34.4	0.45	6	1.73×10^{6}	0.001	55
7540	26.6	0.45	6	1.73×10^{6}	0.001	33
7540	34.4	0.45	6	1.73×10^{6}	0.001	45
35000	34.4	0.1	6	1.73×10^{6}	0.001	81
40000	34.4	0.1	6	1.73×10^{6}	0.001	90
1.00×10^{-5}	55.8	0.45	2	8.50×10^{6}	0	40
1.00×10^{-5}	55.8	0.45	4	8.50×10^{6}	0	79
1.00×10^{-5}	55.8	0.45	6	8.50×10^{6}	0	120
1.00×10^{-5}	55.8	0.45	2	8.50×10^{6}	0.01	40
1.00×10^{-5}	55.8	0.45	4	8.50×10^{6}	0.01	79
1.00×10^{-5}	55.8	0.45	6	8.50×10^{6}	0.01	120
1000	55.8	0.45	2	8.50×10^{6}	0	41
1000	55.8	0.45	4	8.50×10^{6}	0	81
1000	55.8	0.45	6	8.50×10^{6}	0	121
5000	55.8	0.45	2	8.50×10^{6}	0	50
5000	55.8	0.45	4	8.50×10^{6}	0	90
5000	55.8	0.45	6	8.50×10^{6}	0	130
10000	55.8	0.45	2	8.50×10^{6}	0	59
10000	55.8	0.45	4	8.50×10^{6}	0	99
10000	55.8	0.45	6	8.50×10^{6}	0	138

Table E2. Summary of Lebanon Sand drained shear data.

Test no.	Average σ_3 (kPa)	Peak deviatoric stress, *q* (kPa)	Corresponding strain	Max. mean stress, *p* (kPa)	Initial void ratio	Max. volumetric strain
2DS1	14	42	0.18	28	0.53	0.029
2DS2	15	41	0.24	29	0.54	0.028
4DS2	28	76	0.16	52	0.53	0.032
6DS1	43	133	0.19	88	0.54	0.038
6DS2	39	107	0.20	76	0.54	0.039

APPENDIX F. MATERIAL PARAMETERS FOR THAWING LEBANON SAND AND OTHER MATERIALS

The model parameters for the thawing Lebanon Sand are listed in Table F1, along with model parameters from other studies for comparison.

Table F1. Material constants for Capped Drucker–Prager model.

	Lebanon Sand			A-4	Snow* (SNOW2)	McCormick Ranch Sand	Lebanon Sand
Material parameter	**Saturated drained shear**	**Saturated undrained shear**	**13% water content**	**Saturated drained shear**		**Saturated drained shear ****	**Final**
E, Young's modulus, kPa	17250	17440	8490	16000	1379	689475	8500
v, Poisson's ratio	0.32	0.5	0.32	0.33	0.3	0.25	0.32
β, Drucker–Prager angle of friction (º)	55.6	56.4	54.8	53	22.5	14.6	55.8
d, Drucker–Prager material cohesion, kPa	0	0	16.7	16.6	15	1190	10
R, cap eccentricity		0.45 to 0.47	0.45	0.45	1.1×10^{-4}	0.1	0.45
$\varepsilon_{vol}^{pl}\big\vert_0$, initial value of volumetric plastic strain	0.001	0.001	0.001	0.001	0.001	0.001	0
K, flow stress ratio	1.0	1.0	1.0	1.0	1.0	1.0	1.0

* Shoop et al. (1999) and Shoop (2001).

** HKS (1996) and DiMaggio and Sandler (1971, 1976).

REPORT DOCUMENTATION PAGE

Form Approved
OMB No. 0704-0188

1. REPORT DATE *(DD-MM-YYYY)*	**2. REPORT TYPE**	**3. DATES COVERED** *(From - To)*
February 2005	Technical Report	

4. TITLE AND SUBTITLE

Constitutive Model for a Thawing, Frost-Susceptible Sand

5a. CONTRACT NUMBER

5b. GRANT NUMBER

5c. PROGRAM ELEMENT NUMBER

6. AUTHOR(S)

Sally Shoop, Rosa Affleck, Vincent Janoo, Robert Haehnel, and Benjamin Barrett

5d. PROJECT NUMBER

5e. TASK NUMBER

5f. WORK UNIT NUMBER

7. PERFORMING ORGANIZATION NAME(S) AND ADDRESS(ES)

U.S. Army Engineer Research and Development Center
Cold Regions Research and Engineering Laboratory
72 Lyme Road
Hanover, NH. 03755-1290

8. PERFORMING ORGANIZATION REPORT NUMBER

ERDC/CRREL TR-05-3

9. SPONSORING / MONITORING AGENCY NAME(S) AND ADDRESS(ES)

Office of the Chief of Engineers
Washington, DC 20314-1000

10. SPONSOR/MONITOR'S ACRONYM(S)

11. SPONSOR/MONITOR'S REPORT NUMBER(S)

12. DISTRIBUTION / AVAILABILITY STATEMENT

Approved for public release; distribution is unlimited.

Available from NTIS, Springfield, Virginia 22161.

13. SUPPLEMENTARY NOTES

14. ABSTRACT

A material model for soft, wet soil was generated to simulate the deformation behavior of thawing soil under vehicle loading on paved and unpaved roads. Freeze–thaw action produces a loose, wet soil that undergoes large deformation when subjected to vehicle loads. The soil modeled is a frost-susceptible fine sand, which was used in full-scale tests of paved and unpaved road sections in CRREL's Frost Effects Research Facility (FERF). The soil was subjected to a full suite of saturated and unsaturated triaxial testing, using density, moisture, and loading conditions duplicating those experienced during the freeze–thaw testing in the FERF. Material parameters were generated for a capped Drucker–Prager plasticity model. These were calibrated in triaxial test simulations using the commercial finite element code ABAQUS. The material model was then implemented in several three-dimensional finite element simulations for validation and robustness. The model for Lebanon Sand was compared to the same model for other granular materials.

15. SUBJECT TERMS

Frost action
Lebanon Sand
Material properties
Mobility
Soil
Spring thaw
Thaw weakening

16. SECURITY CLASSIFICATION OF:			**17. LIMITATION OF ABSTRACT**	**18. NUMBER OF PAGES**	**19a. NAME OF RESPONSIBLE PERSON**
a. REPORT	**b. ABSTRACT**	**c. THIS PAGE**			**19b. TELEPHONE NUMBER** *(include area code)*
U	U	U	U	75	